



HAL
open science

Dynamics of diabatically-forced anticyclonic plumes in the stratosphere

Aurélien Podglajen, Bernard Legras, Guillaume Lapeyre, Riwal Plougonven, Vladimir Zeitlin, Vincent Brémaud, Pasquale Sellitto

► **To cite this version:**

Aurélien Podglajen, Bernard Legras, Guillaume Lapeyre, Riwal Plougonven, Vladimir Zeitlin, et al.. Dynamics of diabatically-forced anticyclonic plumes in the stratosphere. 2023. hal-04235513v1

HAL Id: hal-04235513

<https://hal.science/hal-04235513v1>

Preprint submitted on 10 Oct 2023 (v1), last revised 6 Nov 2023 (v2)

HAL is a multi-disciplinary open access archive for the deposit and dissemination of scientific research documents, whether they are published or not. The documents may come from teaching and research institutions in France or abroad, or from public or private research centers.

L'archive ouverte pluridisciplinaire **HAL**, est destinée au dépôt et à la diffusion de documents scientifiques de niveau recherche, publiés ou non, émanant des établissements d'enseignement et de recherche français ou étrangers, des laboratoires publics ou privés.

Dynamics of diabatically-forced anticyclonic plumes in the stratosphere

Aurélien Podglajen¹, Bernard Legras¹, Guillaume Lapeyre¹, Riwal Plougonven¹, Vladimir Zeitlin¹, Vincent Brémaud¹, and Pasquale Sellitto^{2,3}

¹LMD/IPSL, École Polytechnique, Institut Polytechnique de Paris, ENS, Université, Sorbonne Université, CNRS

²Laboratoire Interuniversitaire des Systèmes Atmosphériques (LISA-IPSL), Univ. Paris Est Créteil, Université de Paris Cité, CNRS, Institut Pierre-Simon Laplace

³Istituto Nazionale di Geofisica e Vulcanologia, Osservatorio Etneo, Catania, Italy

September 30, 2023

Abstract

A new class of vortices has been observed in the stratosphere after several extreme wildfires (Canada 2017, Australia 2020) and volcanic eruptions (Raikoke 2019). They are long-lived coherent plumes of aerosols and combustion/volcanic compounds confined within mesoscale (100s to 1000 km diameter) anticyclones. Due to their anomalous composition, these ascending anticyclonically-trapped plumes (ATPs) generate significant radiative forcing and diabatically-driven vertical motions. The present paper investigates the fundamental processes shaping the dynamics of ATPs from two complementary approaches: analytically in a potential vorticity (PV) perspective and using idealized but more complete numerical simulations with the Weather Research and Forecast (WRF) model. We adapt the axisymmetric Eliassen balanced vortex model, introduced as a prototype for tropical cyclones, to the case of a vortical flow forced by a diabatically-active Lagrangian tracer. Invoking an extended PV impermeability theorem, it is first clarified that ATP formation is consubstantial to the large injection of mass into the stratified flow at extratropical latitude. We also prove that vertically self-translating, strictly zero-PV ellipsoidal anticyclonic plumes with uniform tracer constitute an exact solution of the governing equations, thus accommodating the joint ascent of tracer and PV in ATPs. The numerical simulations reveal that finite-PV plumes with distributed tracer evolve into a vertically asymmetrical structure featuring a tracer and anticyclonic PV front followed by a tracer tail where cyclonic PV develops. Switching to potential radius-potential temperature coordinate, the dynamics reduces to that of a comb of 1-dimensional Burgers' equation for the tracer, supplemented by a slave equation for PV. By virtue of the symmetry of the problem when neglecting the background density gradient, cooled vortices undergo a similar evolution during their early subsidence, a situation which may apply to the 2022 Hunga Tonga-Hunga-Ha'apai volcanic plume. Finally, the impact of the initial conditions are discussed.

ORIGINAL ARTICLE

Journal Section

Dynamics of diabatically-forced anticyclonic plumes in the stratosphere

Aurélien Podglajen¹ | Bernard Legras¹ | Guillaume Lapeyre¹ | Riwal Plougonven¹ | Vladimir Zeitlin¹ | Vincent Brémaud¹ | Pasquale Sellitto^{2,3}

¹LMD/IPSL, École Polytechnique, Institut Polytechnique de Paris, ENS, PSL Université, Sorbonne Université, CNRS, Palaiseau France

²Univ. Paris Est Créteil and Université de Paris Cité, CNRS, Laboratoire Interuniversitaire des Systèmes Atmosphériques (LISA-IPSL), Institut Pierre-Simon Laplace, Créteil, France

³Istituto Nazionale di Geofisica e Vulcanologia, Osservatorio Etneo, Catania, Italy

Correspondence

Aurélien Podglajen, Laboratoire de Météorologie Dynamique (LMD), École Polytechnique, Palaiseau, 91128, France
Email: aurelien.podglajen@lmd.ipsl.fr

A new class of vortices has been observed in the stratosphere after several extreme wildfires (Canada 2017, Australia 2020) and volcanic eruptions (Raikoke 2019). They are long-lived coherent plumes of aerosols and combustion/volcanic compounds confined within mesoscale (100s to 1000 km diameter) anticyclones. Due to their anomalous composition, these ascending anticyclonically-trapped plumes (ATPs) generate significant radiative forcing and diabatically-driven vertical motions. The present paper investigates the fundamental processes shaping the dynamics of ATPs from two complementary approaches: analytically in a potential vorticity (PV) perspective and using idealized but more complete numerical simulations with the Weather Research and Forecast (WRF) model. We adapt the axisymmetric Eliassen balanced vortex model, introduced as a prototype for tropical cyclones, to the case of a vortical flow forced by a diabatically-active Lagrangian tracer. Invoking an extended PV impermeability theorem, it is first clarified that ATP formation is consubstantial to the large injection of mass into the stratified flow at extratropical latitude. We also prove that vertically self-translating, strictly zero-PV ellipsoidal anticyclonic

plumes with uniform tracer constitute an exact solution of the governing equations, thus accommodating the joint ascent of tracer and PV in ATPs. The numerical simulations reveal that finite-PV plumes with distributed tracer evolve into a vertically asymmetrical structure featuring a tracer and anticyclonic PV front followed by a tracer tail where cyclonic PV develops. Switching to potential radius-potential temperature coordinate, the dynamics reduces to that of a comb of 1-dimensional Burgers' equation for the tracer, supplemented by a slave equation for PV. By virtue of the symmetry of the problem when neglecting the background density gradient, cooled vortices undergo a similar evolution during their early subsidence, a situation which may apply to the 2022 Hunga Tonga-Hunga-Ha'apai volcanic plume. Finally, the impact of the initial conditions are discussed.

KEYWORDS

wildfire plume, volcanic plume, potential vorticity, diabatic heating, geophysical fluid dynamics, stratosphere

1 | INTRODUCTION

While the flow in the midlatitude lower stratosphere is generally characterized by slow diabatic vertical transport (Brewer, 1949; Butchart, 2014), extreme events such as intense pyroconvection from wildfires (Fromm et al., 2010) or large volcanic eruptions (Holasek et al., 1996; Carr et al., 2022) can result in the rapid and direct injection into the stratosphere of air from lower levels loaded with combustion products or volcanogenic compounds. Such injections have the ability to alter stratospheric composition and general circulation for years, as well as have significant impacts on the global radiative budget (Schallock et al., 2023).

For a few years, it has been recognized that stratospheric plumes may feature specific meso-scale dynamics. A typical example is the plume from 2019-2020 Australian wildfires which self-organized into several long-lived coherent smoke bubbles. Such bubbles, typically a few kilometer deep and hundreds of kilometer wide, experienced an ascent in the mid-latitude stratosphere while maintaining a compact structure (Khaykin et al., 2020; Kablick et al., 2020; Pumphrey et al., 2021). Atmospheric reanalyses revealed that the preservation of those ellipsoidal structures against stirring and dilution by the large-scale flow resulted from the confinement of the plume within anticyclonic vortices. The largest of those anticyclonically-trapped plume (ATP) patches was associated with a 1000-km diameter vortex, and remained visible as an ascending isolated bubble of ash for 3 months, rising from 16 to 36 km. Since then, similar smoke anticyclones have been identified retrospectively in the aftermath of the 2017 wildfires in British Columbia (Lestrelin et al., 2021). In both cases, diabatic lofting of the smoke plume reaching several degrees of potential temperature per day (e.g., Boers et al., 2010; de Laat et al., 2012; Khaykin et al., 2018; Yu et al., 2019; Khaykin et al., 2020) was attributed to the absorption of incoming solar radiation by black carbon aerosols. A similar phenomenon may

1
2 have taken place in the ash-rich aerosol cloud from the 2019 eruption of the ash-enriched Raikoke volcano (Khaykin
3 et al., 2022b), which organized into horizontally circular patches (Cai et al., 2022) and ascended from 18 to 25 km in
4 the course of a few months (Chouza et al., 2020).

5
6 More recently, the eruption of the Hunga Tonga-Hunga Ha'apai volcano generated the largest and highest strato-
7 spheric injection since at least the eruption of Mount Pinatubo in 1991, with the main detrainment located around
8 35 km altitude (Carr et al., 2022; Proud et al., 2022). This time, the perturbation in the composition consisted of sulphur
9 compounds and water vapor (Millán et al., 2022; Khaykin et al., 2022a), and the latter generated substantial in-plume
10 diabatic cooling and a rapid descent (Sellitto et al., 2022). Although this feature was not captured by the ECMWF
11 operational analyses, Legras et al. (2022) noticed using a suite of space-borne instruments that the plume tended to
12 roll-up over the weeks following the eruption and exhibited a wind anomaly corresponding to anticyclonic vorticity.
13 Such long-lasting (several weeks) anticyclonic rotation is distinct from that resulting from the initial adjustment of the
14 plume after it reaches its level of neutral buoyancy (e.g., Baines and Sparks, 2005).

15
16 Whereas for adiabatic motions the role of vorticity in isolating plumes and preserving them from dilution within
17 the environment corresponds to a well-known property of geophysical flows (e.g., Schoeberl et al., 1992; Garny
18 and Randel, 2013), the processes behind the formation and evolution of diabatically-forced ATPs remain somewhat
19 unclear in the literature. By introducing sunlight-absorbing aerosols in the upper troposphere in the GEOSCCM global
20 model, Doglioni et al. (2022) were able to numerically simulate smoke-charged vortices. However, if their study
21 demonstrates the robustness of the mechanisms at play, the authors did not provide an explanation for the observed
22 dynamics. Lestrelin et al. (2021) carefully analyzed the dynamical structure of Australian and Canadian smoke vortices
23 in CALIOP spaceborne lidar observations and the ERA5 reanalysis. They found that the anticyclone-trapped smoke
24 plumes had broad ellipsoidal shapes, with a vertical-to-horizontal aspect ratio on the order of f/N where f and N
25 are the Coriolis and Brunt-Väisälä frequencies. Analysed winds and temperature are consistent with the structure of
26 an anticyclone. Interestingly, at the center of the anomaly, the ERA5 was found to diagnose almost vanishing (nearly
27 zero) absolute vorticity, which in the midlatitude stratosphere is unlikely result solely from the adiabatic evolution of
28 the flow.

29
30 Lestrelin et al. (2021) proposed to interpret low absolute-PV smoke anticyclones as resulting from the vertical
31 transport of smoke-charged tropospheric air bubbles conserving both their low PV and their tropospheric tracer con-
32 tent during their diabatic ascent to and through the stratosphere. This conjecture was used by Khaykin et al. (2022b) to
33 explain the confinement and anticyclonic motion of the Raikoke volcanic plume. Nevertheless, the theory presented
34 by Lestrelin et al. (2021) is incomplete from a dynamical point of view, as recognized by the authors themselves : by
35 considering Lagrangian conservation of PV, it ignores the central contribution of diabatic heating to its evolution (e.g.
36 Hoskins et al., 1985; Haynes and McIntyre, 1987).

37
38
39 The goal of the present paper is to investigate the dynamics governing the formation and maintenance of cooled
40 and heated ATPs and in particular their connection with the dynamics of potential vorticity in a diabatically-forced
41 flow. We will describe a conceptual model based on theoretical considerations and numerical simulations. The article
42 is organized as follows. In Sect. 2, we revisit the observational evidence for plume vortices and highlight particular
43 dynamical properties. In Sect. 3, we recall the theory of potential vorticity dynamics in diabatically forced axisymmetric
44 flow and derive a set of simplified equations describing the joint evolution of potential vorticity and a diabatically-
45 active tracer. A particular solution to the problem of a co-ascending tracer and PV patch is introduced. Section 4
46 presents results from numerical simulations with a heated and cooled tracer plume and then Section 5 provides a
47 discussion. Conclusions and recommendations for future work are outlined in Sect 6.

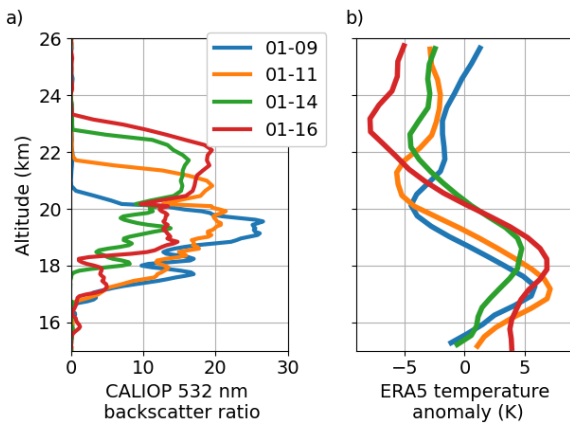


FIGURE 1 (a) Vertical profiles of the 532 nm CALIOP (attenuation-corrected) backscatter ratio across Koobor at the latitude of the associated vortex center for 4 night orbits between 9 and 16 January 2020 chosen for the proximity of the CALIOP orbit to the vortex. (b) Colocated ERA5 temperature zonal anomaly profiles.

2 | OBSERVATIONS OF THE 2020 KOOBOR SMOKE-CHARGED VORTEX

Observations are revisited to highlight some special properties of the aerosol cloud and associated vortex from the 2020 Australian wildfires which have not been emphasized in previous studies. We process the 532 nm total attenuated backscatter data from the spaceborne lidar CALIOP (Cloud-Aerosol lidar with Orthogonal Polarization) onboard the CALIPSO satellite (Vaughan et al., 2004; Winker et al., 2010). We use version 4.50 (Kar et al., 2018; Getzewich et al., 2018) of the level 1 product. Global Navigation Satellite System (GNSS) radio occultation (RO) temperature soundings are obtained from "dry retrievals" from the COSMIC Data Analysis and Archive Center (CDACC) website <https://cdaac-www.cosmic.ucar.edu/>. Other temperature and potential vorticity fields are derived from the ERA5 reanalysis (Hersbach et al., 2020).

Vertical cross-sections of attenuated backscatter ratio from CALIOP were instrumental in the discovery of stratospheric plume vortices (Khaykin et al., 2020). The main vortex, nicknamed Koobor in reference to an aboriginal legend (Lestrelin et al., 2021), could be followed over three months in the stratosphere with the lidar. Figure 1 displays profiles of backscatter ratio at the center of the smoke plume from selected CALIOP cross-sections between 9 to 16 January 2020, i.e. during the early phase of Koobor's life when it was horizontally stagnating over the Pacific but rising rapidly from 19 to 22 km, an altitude range with limited shear. The sections were selected based on a criterion of proximity with the location of the vortex center according to the ERA5 reanalysis. An extended view including full sections and horizontal potential vorticity maps showing how CALIPSO tracks intersect the vortex is shown in Fig. 2.

In Fig. 1, the (attenuation-corrected) backscatter ratio, that is the ratio of the particular backscatter over the molecular backscatter, is computed from the measured total attenuated backscatter profile and theoretical molecular backscatter (Vaughan et al., 2004). The lidar ratio (assumed constant) needed for the inversion is estimated for each profile using the constraint provided by the attenuation of the molecular backscatter signal in the clear-sky stratosphere below the smoke cloud. The range of 532 nm lidar ratios thus deduced lie between 50 and 75, on the lower side of the values reported by Ohneiser et al. (2020) for the 2020 Australian smoke plume. The advantage of using backscatter (instead of the raw attenuated backscatter in Fig. 2) is that, provided that the microphysical and optical

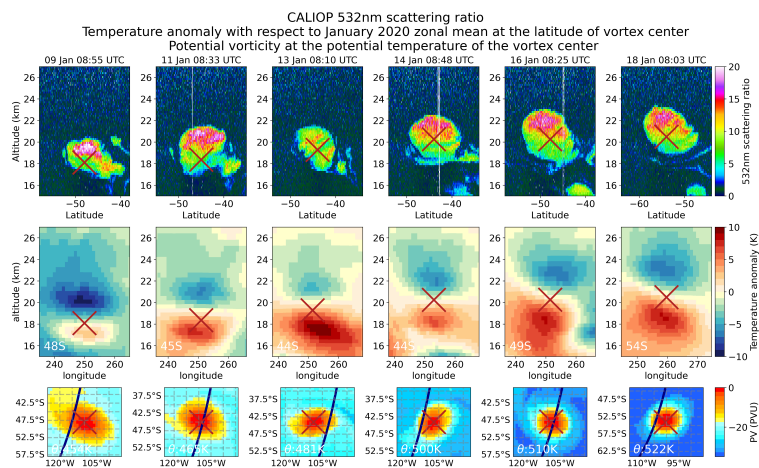


FIGURE 2 Top row: sections of 532 nm CALIOP attenuated scattering ratio corresponding to the profiles of Fig. 1. The crosses indicate the altitude and latitude of the associated vortex in ERA5. Middle row: corresponding vertical sections of ERA5 temperature in the zonal direction at the latitude of the vortex center. The cross indicates the altitude and longitude of the vortex center. Bottom row: Horizontal chart of potential vorticity at the altitude of the vortex centre shown by the cross.

properties of the particles (e.g., their size) are uniform throughout the cloud, backscatter ratios may be interpreted as proportional to the mixing ratio of the aerosols.

As noted in previous studies, backscatter ratio profiles evidence a rise of the plume with time; according to the ERA5 reanalysis, the aerosol cloud is accompanied along its ascent by a temperature dipole associated with the anticyclonic vortex with the cold anomaly topping the warm anomaly. Figure 1 further illustrates an interesting aspect: the aerosol profiles exhibit a seasaw shape with a sharp front ascending at the top of the cloud and a slowly sloping (and sometimes perturbed) tail trailing behind. Although this interpretation is likely complicated by shear and possibly by sedimentation, the bottom of the cloud seems to rise more slowly than its top. This differential ascent speed results in an increase of the vertical extent of the plume with time. Figure 1b shows that the minimum of temperature anomaly is located at the front of the aerosol seasaw while the maximum gets broader with time as the aerosol tail develops.

In this oceanic area void of radiosonde stations, the ERA5 reanalysis was mostly informed by the assimilation of satellite temperature observations. The capacity of the assimilation system to follow the temperature profiles is illustrated in Fig. 3 for a remarkable encounter between Koobor and one of its siblings, denoted as vortex V2, that occurred on 15 January 2020. Koobor formed after the intense phase of pyroconvection on 29–31 December 2019 while V2 originates from the event of 4 January 2020 (Peterson et al., 2021). Figure 3a shows the two clouds superimposed in a single section of CALIOP. Figure 3c shows the track of the CALIPSO orbit which crosses the two vortices between their two centers and also the location of 3 selected GPS radio-occultation soundings located within 6 arc degrees of both vortices. Figure 3b compares the ERA5 temperature profiles at the location of the two vortices and from the 3 GPS soundings. The superposition of the two vortices generates a double temperature dipole, which the ERA5 is able to follow event with remarkable fidelity. As shown in Khaykin et al. (2020), another source of temperature information is provided by the infrared sounders, mainly the IASI instruments on board the Metop platforms. This ability of the reanalysis to accurately reproduce the temperature signature does not mean that all meteorological fields are

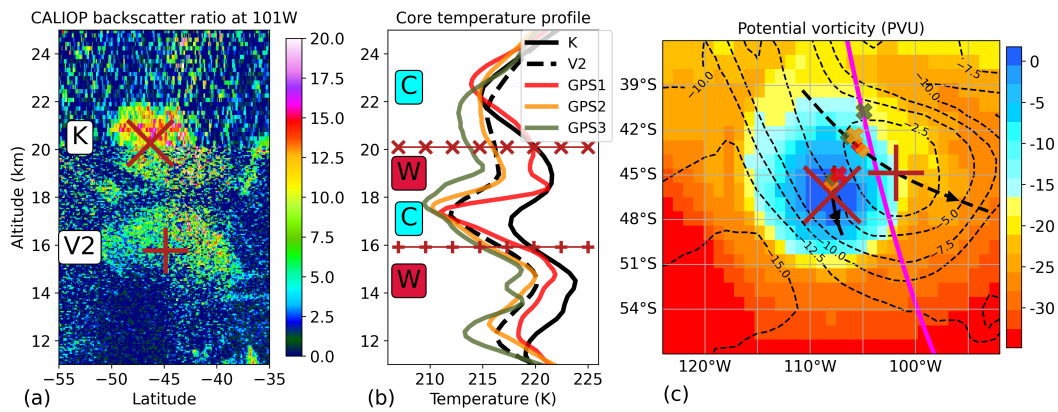


FIGURE 3 (a) Daytime CALIOP 532 nm total attenuated backscatter ratio on 15 January 2020 at 21:03 UTC (time J). The two crosses indicate the latitude and altitude centers of Koobor (K) and the 2nd vortex (V2) in the ERA5, (b) Vertical profiles of the ERA5 temperature at the location of the two vortices (in black) and temperature profiles from three nearby GPS soundings on 15 January denoted as GPS1 (KOMPSAT5, 14:29 UTC), GPS2 (COSMIC2, 15:22 UTC) and GPS3 (TSX, 12:32 UTC). The selected profiles are distant from both vortices by less than 600 km. The lines with crosses indicate the altitude of the two vortices, 20.1 km for Koobor and 15.9 km for V2 (c) ERA5 potential vorticity maps of Koobor (colour) and V2 (contours) at the isentropic level of their center (503 K for Koobor and 408 K for V2). The black lines indicate the trajectories of the two vortices in the interval $[J-18h, J+18h]$. The large crosses indicate the location of the two vortices at time J, like in (a). The locations of GPS soundings is shown as crosses (colours as in (b)) and the location of each vortex along its trajectory at the time of the sounding is shown by a diamond.

equally reliable. While the reconstructed potential vorticity pattern appears as a large ball of the size of the aerosol cloud, with near zero potential vorticity (PV) at its center (Lestrelin et al., 2021), the exact shape and magnitude of the PV bubble is not directly constrained by the observations assimilated in ERA5. Such property of low PV (which places the vortex on the verge of symmetric instability) is surprising and worthy of further theoretical and numerical investigations.

3 | THEORY

3.1 | Potential vorticity budget of an axisymmetric flow

Given their typical scales, ATPs in rotating stratified fluids can be studied using tools from potential vorticity theory (Hoskins et al., 1985). As a first approximation, they can be considered axisymmetric structures, a geometry motivated by the observations (see Fig. 3). Isolated axisymmetric vortices are a long-studied topic of fluid mechanics. Regarding atmospheric applications, Eliassen (1952) introduced the model of a quasi-stationary axisymmetric vortex, sometimes referred to as the Eliassen balanced vortex model (Schubert and Hack, 1983). His seminal work was later developed to investigate tropical cyclones dynamics from the point of view of potential vorticity (see, e.g., Schubert, 2018, and references therein). In the following, we will rely on a framework introduced by Schubert and Alworth (1987) and Schubert (2018) for tropical cyclones, adapting it to the case of ATPs.

The fundamental starting point is the dynamics of Ertel's potential vorticity (PV) (Ertel, 1942), which is expressed

in cartesian coordinate as:

$$P = \frac{1}{\rho} \zeta_a \cdot \nabla \theta \quad (1)$$

where ρ is the density, θ the potential temperature and ζ_a the absolute vorticity vector. In an inviscid (i.e., neglecting non-conservative mechanical forcings) adiabatic flow, the potential vorticity (PV), noted P , is materially conserved. This is the base of the analogy between PV and tracers. In the case of vortices subject to heating and mechanical forcing, Lagrangian conservation of P is no longer guaranteed. In cartesian coordinate, the PV evolution equation reads (e.g., Andrews et al., 1987):

$$\frac{DP}{Dt} = \frac{1}{\rho} \zeta_a \cdot \nabla Q + \frac{1}{\rho} \nabla \theta \cdot \nabla \times \mathbf{F} \quad (2)$$

with $Q = D\theta/Dt = \theta$ the diabatic heating rate as potential temperature tendency and \mathbf{F} the mechanical forcing.

In the following, we restrict ourselves to the case of an axisymmetric flow on the f -plane where f is the Coriolis parameter. With r the radial coordinate, u , v the components of the horizontal wind in the radial and azimuthal directions, respectively, PV may be expressed as (e.g. Shutts, 1991; Schubert, 2018):

$$P = \frac{f}{2\rho r} \left(\frac{\partial(R^2, \theta)}{\partial(r, z)} \right) = \frac{f}{2\rho r} \left(\frac{\partial R^2}{\partial r} \frac{\partial \theta}{\partial z} - \frac{\partial R^2}{\partial z} \frac{\partial \theta}{\partial r} \right) \quad (3)$$

where we introduce the notation $\left(\frac{\partial(a,b)}{\partial(x,y)} \right) = \frac{\partial a}{\partial x} \frac{\partial b}{\partial y} - \frac{\partial a}{\partial y} \frac{\partial b}{\partial x}$ for the Jacobian determinant and R is the potential radius (e.g. Schubert and Hack, 1983), which is related to the absolute angular momentum and defined as:

$$\frac{1}{2} f R^2 = rv + \frac{1}{2} f r^2. \quad (4)$$

As may be deduced from the azimuthal momentum equation (Eq. A1), Lagrangian changes in R arise solely due to drag in the azimuthal direction F_λ :

$$\frac{DR}{Dt} = R = \frac{r}{Rf} F_\lambda. \quad (5)$$

Hence, R has the interesting property of Lagrangian conservation in an axisymmetric flow without mechanical forcing ($\mathbf{F} = 0$).

To simplify the equations further, a convenient and commonly-employed change of coordinates consists in switching to potential radius R as horizontal coordinate (e.g. Shutts and Thorpe, 1978; Thorpe, 1985) together with potential temperature θ as vertical coordinate (e.g., Schubert and Alworth, 1987). Such coordinate transformation requires that there exists a bijective mapping from (r, z) to (R, θ) , which is guaranteed as long as $P > 0$, i.e. as long as the flow is stable with respect to symmetric instability. If it exists, a region of the fluid with $P = 0$ (symmetrically-neutral air) maps out into a line in $R - \theta$ space and the coordinate transformation is no longer bijective. μ is then a Dirac in $(R - \theta)$ space, collapsing to a line along the R -coordinate (convectively neutral) or the θ coordinate (inertially neutral). Recalling the mathematical property that the Jacobian determinant represents the change in differential volume under coordinate

transformation, the infinitesimal volume element is given by:

$$dV = \pi dr^2 dz = \frac{\pi}{\frac{1}{2r} \left(\frac{\partial(R^2, \theta)}{\partial(r, z)} \right)} dR^2 d\theta. \quad (6)$$

and the corresponding mass reads:

$$dM = \rho dV = \rho \pi dr^2 dz = \frac{\pi}{\frac{1}{2\rho r} \left(\frac{\partial(R^2, \theta)}{\partial(r, z)} \right)} dR^2 d\theta. \quad (7)$$

Hence, the density μ in the (R, θ) coordinate system, termed potential density by Schubert and Alworth (1987), relates to PV through:

$$\mu = \frac{1}{\frac{1}{2\rho r} \left(\frac{\partial(R^2, \theta)}{\partial(r, z)} \right)} = \frac{f}{P} \quad (8)$$

(given the definition of P in Eq. 3). In particular, Equation 8 shows that μ is inversely proportional to P . Consequently, the PV evolution equation (Eq. 2) in this system:

$$\frac{\partial P}{\partial t} + R \frac{\partial P}{\partial R} + Q \frac{\partial P}{\partial \theta} = P \left(\frac{1}{R} \frac{\partial(RR)}{\partial R} + \frac{\partial Q}{\partial \theta} \right) \quad (9)$$

has the following flux-form :

$$\frac{\partial \mu}{\partial t} + \frac{1}{R} \frac{\partial(RR\mu)}{\partial R} + \frac{\partial(Q\mu)}{\partial \theta} = 0, \quad (10)$$

which is the continuity equation in (R, θ) coordinate.

It is enlightening to put this equivalence between PV and inverse $R - \theta$ pseudo-density μ in the perspective of the PV impermeability theorem of Haynes and McIntyre (1987, hereafter HM87). HM87 showed that the (Eulerian) evolution equation of the quantity $\rho P = \zeta_a \cdot \nabla \theta$ may be recast into a flux-form budget equation in geometric coordinate- (x, y, z) or, in particular here, (r, z) :

$$\frac{\partial \rho P}{\partial t} + \nabla \cdot \mathbf{J} = 0 \quad (11)$$

with \mathbf{J} being the flux of PV substance. On this ground, they proposed an analogy between PV and chemical substances, namely that the quantity ρP be seen as the concentration of a PV substance (PVS) of mixing ratio P . HM1987 then proved that, contrary to fluid mass or chemical substances, there is no net flux \mathbf{J} of PVS across isentrope surfaces even in the presence of diabatic heating and friction/viscous stress. This result, named the impermeability theorem, follows solely from the definition of PV; in particular, it does not rely on the equations of motion.

For our axisymmetric problem, Equation 8 may be viewed as an extension of the HM87 impermeability theorem for f/P to both iso- θ and iso- R (iso-angular momentum) surfaces. Here, the iso- θ result is the standard impermeability theorem while the iso- R component is a consequence of the definition of the R coordinate. The name impermeability here refers to the absence of net PVS flux across R and θ contours, which again specifically applies to the "mass" of PVS but not to the mass of fluid nor the mass of another tracer. Such framework offers a convenient interpretation of PV, sometimes referred to as the dilution/concentration principle. The mass of PV substance contained in a volume

delimited by iso- R and iso- θ surfaces is fixed in time: PV can only be diluted by mass convergence - or concentrated by mass divergence. In the case of mass convergence, dilution of PVS leads to the formation of anticyclonic PV, resulting in the expansion of R and theta contours in physical space. The reverse occurs for mass divergence, leading to contraction of R and theta contours in physical space. Conversely, if we consider a closed material contour C and follow it in time, the (R, θ) volume $\int \int \pi dR^2 d\theta$ enclosed by C , i.e. the mass of PVS, is trivially proportional to the average PV within the contour (since mass is conserved).

3.2 | Relationship between PV and mass injection and the 0-PV limit case

The relation between PV and mass redistribution in rotating fluids is not new. Considering the Lagrangian conservation of θ and R , Gill (1981) suggested the inviscid and adiabatic adjustment of a fluid injection as a way to create anticyclones in rotating stratified flows, a method first applied in rotating tank experiments by Griffiths and Linden (1981) and used in a number of studies since then (e.g., Aubert et al., 2012). A similar reasoning was employed to understand the atmospheric adjustment to penetrative convection (e.g. Shutts et al., 1988).

Based on the correspondence between mass anomaly in $R - \theta$ and PV, the fraction of mass injected $((\mu_i - \bar{\mu})/\mu_i)$, which may be used to define the initial mixing ratio of a plume tracer χ_i , can be expressed as a function of PV:

$$\chi_i(x, y, \theta) = \frac{\mu_i(x, y, \theta) - \bar{\mu}(\theta)}{\mu_i(x, y, \theta)} = \frac{\bar{P}(\theta) - P_i(x, y, \theta)}{\bar{P}(\theta)} \quad (12)$$

where $\bar{P}(\theta) = f/\bar{\mu}$ is the potential vorticity of the background state and $\bar{\mu}$ the corresponding density in (R, θ) coordinates.

A special case arises when $P = 0$ in an extended region: the area with $P = 0$ in (r, z) collapses to a line in (R, θ) coordinate. If the initial 0-PV is realized through $\zeta_a = 0$, then, in a frictionless flow, potential vorticity remains zero even in the presence of diabatic forcing (see Eq. 2 and Eq. 13). This is connected to the general property of a perfect fluid that an irrotational flow remains irrotational at all times. This maintenance of the 0-PV raises the question of the existence of vertically translated solutions conserving their shape and preventing the tracer from being diluted within the environment. In Appendix A1, it is proven that such exact solutions do exist for a variety of (axisymmetric) geometric configurations of the PV/tracer patch and background when there is no tracer diffusion nor viscosity. The self-translating solution has both heating rate and tracer mixing ratio uniform and collocated with the 0-PV patch, and a strictly 0 PV. Whereas this points to the importance of vanishing PV in the maintenance of the PV tracer cloud along its vertical ascent and suggests that axisymmetry may be preserved, such academic solution is of limited practical interest. In the following, we investigate the evolution of a finite (albeit small) PV and tracer injection.

3.3 | Flow response to a heated tracer for a finite PV

In the remainder of this section, we will assume $R = 0$ (i.e., we neglect mechanical forcing). Following Eq. 5, the PV dynamics may then be reduced to that of a comb of (vertical) 1-D domains on R -rings, with each R -ring independent of its neighbor. In such case, Lagrangian evolution of PV reads:

$$\frac{DP}{Dt} = PQ_\theta \quad (13)$$

with $Q_\theta = \left(\frac{\partial Q}{\partial \theta}\right)_R$ and it is now understood that $D_t P = \partial_t P + Q \partial_\theta P$. The solution to Eq. 13 along characteristics reads: $P(\tau) = P_0 \exp \int_0^\tau Q_\theta d\tau'$ and highlights exponential growth/decay of the PV with time for constant Q_θ , as noted by Schubert and Alworth (1987).

Let us consider the diabatically forced 1-D system in which PV is coupled with a radiatively active but chemically inert tracer, which will be referred to as tracer A (for active). To the best of our knowledge, this configuration has never been explored. We assume that A is inert and its mixing ratio χ obeys a form of 1-D advection-diffusion equation in (R, θ) coordinate:

$$\frac{D\chi}{Dt} = \mathcal{D}(\mu, \chi) \quad (14)$$

where \mathcal{D} is a diffusion operator (linear in χ). Under this simplification, it is not trivial how to appropriately parameterize the diffusive term on the right-hand side of Eq. 14 (which is necessary for the unicity of the results). \mathcal{D} does not account for molecular diffusion, but rather represents the effect of turbulent mixing which may be associated with either a population of intermittent turbulent patches (e.g. Vanneste and Haynes, 2000) not directly related to the flow dynamics, or the formation of dynamic instabilities, such as symmetric instability, whose development tends to relax the flow towards a state of neutrality. A priori, $\mathcal{D}(\mu, \chi)$ is anisotropic but will induce both cross- R and cross- θ fluxes.

To gain further insight, we note that, when neglecting tracer diffusion ($\mathcal{D} = 0$ in Eq. 14),

$$\frac{1}{P} \frac{DP}{Dt} = \frac{\partial Q}{\partial \theta} = -\frac{1}{\chi_\theta} \frac{D\chi_\theta}{Dt} \quad (15)$$

where $\chi_\theta = \left(\frac{\partial \chi}{\partial \theta}\right)_R$. This holds for any form of the heating. In such a case, along Lagrangian characteristics (material trajectories):

$$P \chi_\theta = P(t=0) \chi_\theta(t=0) \quad (16)$$

Potential vorticity in this system is inversely proportional to the tracer gradient, a property which may be interpreted using the (R, θ) version of the PV impermeability theorem: since without diffusion tracer isopleths follow material trajectories, the convergence of isopleths (relative increase in χ_θ) is associated with the convergence of fluid mass and the dilution of PV, whereas the divergence of isopleths leads to the concentration of PV. Strictly speaking, relation (16) only holds before overturns (change of sign of χ_θ , i.e. intersection of characteristics) occur and shows that we expect anticyclonic (low) PV to develop where tracers gradients are steepening.

As a first approximation, we will assume that the anomaly in heating rate \mathcal{H} induced by the active tracer A is proportional to its mixing ratio χ and of the form:

$$\mathcal{H} = \gamma \chi \quad (17)$$

where γ is a constant factor and the heating rate \mathcal{H} corresponds to the temperature tendency $\mathcal{H} = T = \frac{T}{\theta} Q$. Equation 17 encapsulates the linear relationship between \mathcal{H} , extinction ratio and tracer mixing ratio in the case of constant and uniform radiative (and microphysical) properties of the tracer. However, it neglects any substantial attenuation of the radiative flux which could arise in thick plumes. In the case of the biomass burning plumes from the 2020 Australian fires, absorption of sunlight by black carbons is modeled by $\gamma > 0$ and the assumption of neglecting attenuation appears reasonable since CALIOP reveals only partial attenuation of the lidar beam at 532 nm (Sect. 2). Furthermore, regarding the radiative properties of the emitted black carbon particles, it was recently observed by

Sellitto et al. (2023) that they remained quite stable over time scales of weeks to months. This justifies Eq. 17 at first order, although for longer times microphysical and chemical processes will likely result in a contrasted evolution of the radiative properties of the tracer in different parts of the plume. Furthermore, it should be emphasized that, besides simplifying the heating induced by the absorbing/emitting layer, Equation 17 also ignores the thermal damping of the deviation of temperature from its background profile due to the PV anomaly. This component is left out for now but will be included in Sect. 4.

Equation 17 yields for the potential temperature tendency Q :

$$Q = \frac{\gamma}{\bar{\Pi}} \chi \approx \frac{\gamma}{\bar{\Pi}(\theta)} \chi \quad (18)$$

where the dimensionless Exner function $\Pi = \frac{T}{\theta}$ is related to the distribution of PV and a priori depends on time, R and θ , but may in practice be replaced by its background profile $\bar{\Pi}(\theta)$. With those approximations, Lagrangian conservation of the tracer mixing ratio in (R, θ) coordinate including tracer diffusion reads:

$$\frac{\partial \chi}{\partial t} + \frac{\gamma}{\bar{\Pi}} \chi \left(\frac{\partial \chi}{\partial \theta} \right)_R = \mathcal{D}(\mu, \chi). \quad (19)$$

After a change of the vertical coordinate to $\Theta(\theta) = \int_{\theta_{ref}}^{\theta} \frac{\bar{\Pi}(\theta')}{\gamma} d\theta'$, Equation 19 reduces to Burgers' equation, which constitutes a canonical example of non linear waves and has been extensively studied. It admits exact analytical solutions (e.g. Hopf, 1950; Cole, 1951) for $\mathcal{D}(\mu, \chi) = K \partial_{\Theta}^2 \chi$ with constant "diffusivity" K . For a detailed presentation, we refer the reader to standard textbooks on partial differential equations (e.g. Whitham, 1999) and only provide in the following a brief account of the behavior of the tracer solutions to our problem and the associated PV profile.

In the limit of vanishing diffusion ($\mathcal{D}(\mu, \chi) \rightarrow 0$), Burgers' equations may be fully solved along characteristics. Starting from an initial value of the tracer slope $(\chi_{\theta})_0 > 0$ and following the characteristic, χ_{θ} and potential vorticity P evolve with time as $\chi_{\theta} = (\chi_{\theta})_0 (\bar{\Pi}_0/\bar{\Pi}) (1 - (t/\tau_s))^{-1}$ and $P = (1 - (t/\tau_s)) (\bar{\Pi}/\bar{\Pi}_0) P_0$ with $\tau_s = -(\gamma(\chi_{\theta}/\bar{\Pi})_0)^{-1}$. Whereas this solution remains continuous at all time on the lower side of the tracer cloud ($\gamma(\chi_{\theta})_0 < 0$), on the upper side ($\gamma(\chi_{\theta})_0 > 0$) the nonlinear advection term causes singularity (multivalued tracer profile) to occur at a finite time τ_s as characteristics intersect and the PV reaches 0. At this point, which corresponds to shocks and overturns in the physical system, diffusive processes comes into play ; it is still possible to construct physically acceptable ("vanishing viscosity") discontinuous solutions to the tracer equation by requiring that Rankine-Hugoniot jump conditions be satisfied at the discontinuity, where PV is strictly 0. For practical applications, it may be desirable to circumvent the formation of the singularity by introducing a diffusion operator, for instance of the form $\mathcal{D} = K \partial_{\Theta}^2 \chi$ where $K > 0$ is a small yet non vanishing diffusivity. Then, the formation of the singularity is prevented and the shock is stabilized as a tracer front of finite width in $\Theta \sim K/(\gamma \chi_{max})$, but for small enough diffusivity (compared to $\int \gamma \chi d\Theta$) this does not affect the location and magnitude of the jump which remain independent of the exact value of K . Still, as a result of Eq. 13, the PV decreases exponentially in the area of the front. This behavior is investigated in detail in Appendix A2, where an analytical solution to the PV Equation is provided for the case of a steadily propagating tracer front.

In order to now examine the full dynamics of the system in (R, θ) , a comb of 1-D Burgers' equations (19) for the tracer and Eq. (13) for the PV is solved along characteristics for the initial condition described in the following. With a background flow at rest, the reference density is simply $\bar{\mu} = \frac{\bar{p}}{(\frac{\partial \theta}{\partial z})_r}$; we assume an isothermal profile at 220 K. The distribution for χ_i is designed to be smoothly varying in R and θ , with compact support and using cosine functions to

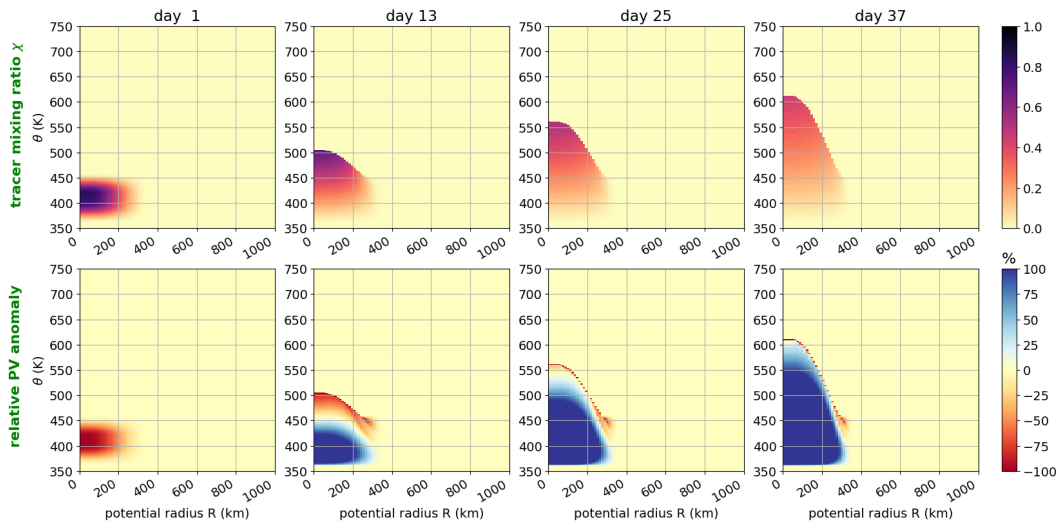


FIGURE 4 Numerical solution of a comb of Burgers' equations along θ with $\gamma = 5 \text{ K/day}$ (unit tracer mixing ratio), starting from the initial condition given in Eq 20 and a background PV profile typical of the mid-latitude. The top row shows the mixing ratio tracer of tracer A the bottom row the PV anomaly. Similar conditions are also used for initialisation and background in the reference WRF simulation. The problem is solved along characteristics, with the front ascent speed and tracer step determined from the Rankine-Hugoniot jump condition.

describe the bulge initial condition in χ_i :

$$\chi_i(r, \theta) = 0.25 \left(1 + \cos\left(\frac{\pi r}{R_{max}}\right) \right) \left(1 - \cos\left(\frac{2\pi(\theta - \theta_{min})}{\theta_{max} - \theta_{min}}\right) \right) \text{ if } r < R_{max} \text{ and } \theta \in [\theta_{min}, \theta_{max}]$$

$$= 0 \text{ otherwise} \tag{20}$$

In the case of the main 2020 Australian vortices, we take guidance from the ECMWF ERA5 reanalysis on 9 January 2020 to estimate the magnitude and size of the injection in (R, θ) coordinate, which suggests $R_{max} = 180 \text{ km}$ and $\theta_{min} = 380 \text{ K}$ and $\theta_{max} = 440 \text{ K}$. The choice for the amplitude, 0.25, is such that the maximum value (reached for $r = 0$ and $\theta = (\theta_{min} + \theta_{max})/2$) is $\chi_i = 1$, corresponding to a vanishing PV ($P_i = \bar{P}(1 - \chi_i) = 0$) at the maximum of the tracer distribution.

The solution for a range of potential radii R is displayed in Figure 4 and illustrates the gradual evolution of the tracer structure from an initially vertically symmetric towards the strongly asymmetric triangular wave with a front sharpening at the top and a smooth tail at the bottom of the tracer cloud. After its formation, the front asymptotically ascends as \sqrt{t} in Θ coordinate whereas the magnitude of the jump decays as $t^{-1/2}$. The varying ascent speed of the discontinuity as a function of R mirrors the initial R -profile of the maximum of tracer concentration along the vertical $\chi_{max}(R)$, following the prescribed heating $\gamma\chi_{max}(R)$. Even more interesting is the evolution of the PV field (bottom row). Starting from the PV distribution defined by Eq. 20, the anticyclonic PV is initially preserved and ascends together with the largest tracer anomaly. At later stages, a positive PV anomaly develops in the tail of the plume whereas the low PV-anomaly at the tracer front is locally strongly enhanced, in agreement with Eq. 15.

The above analysis provides insights on the existence and persistence of anticyclonically-trapped plumes, in particular regarding their initial formation, the co-ascent of a heated tracer and anticyclonic PV patch and the formation

1
2 of a front at the top of the tracer cloud. Given the degree of idealization, it is noteworthy that these seem consis-
3 tent with observed features of ATPs. There are however significant differences between real flows and the modeling
4 above: most conclusions drawn rely on the coordinate transformation to $R - \theta$, which implicitly assumes that the ini-
5 tial axisymmetry of the flow is preserved during its evolution. This is far from guaranteed, as we saw that the system
6 has the intrinsic tendency to produce shocks. Here, shocks were kept and treated explicitly with Rankine-Hugoniot
7 conditions. However, in reality, such situation may first lead to 3D dynamical instabilities, and most likely result in the
8 diffusion of tracer across both θ and R surfaces.

9 Another disadvantage of the $R - \theta$ framework is its relative lack of flexibility and the difficulty to incorporate a more
10 realistic diabatic forcing. In particular, it is expected that the temperature anomaly associated with the anticyclonic PV
11 induces significant thermal relaxation (Lestrelin et al., 2021). This introduces a two-way coupling between potential
12 vorticity and tracer equations: in order to determine a priori this extra heating term, it would be necessary to assume a
13 balance equation for the flow and to invert the temperature anomaly from PV. While there exist numerical methods to
14 solve the PV inversion problem in this cylindrical geometry (e.g. Thorpe, 1985), they are involved and cannot address
15 the question of stability. As an intermediate framework between analytical approaches and real-case simulations, we
16 therefore turn to fully 3D idealized numerical simulations, in which thermal relaxation can be readily included and the
17 validity of the underlying assumptions tested.
18
19
20
21
22
23
24
25
26
27
28
29
30
31
32
33
34
35
36
37
38
39
40
41
42
43
44
45
46
47
48
49
50
51
52
53
54
--

4 | TRIDIMENSIONAL NUMERICAL SIMULATIONS

In this section, we investigate the evolution of an injection of active tracer A with a different approach, including more complete dynamics, but keeping to the realm of idealized approaches. Instead of retaining only PV as the sole descriptor of the flow, we wish to include more complete dynamics. The problem may be summarized as follows: we consider a background atmosphere initially at rest on the f -plane. The chosen Coriolis parameter ($f = 10^{-4} \text{ s}^{-1}$) and background stratification profile mimic the typical midlatitude troposphere-stratosphere transition, with a tropopause located at 12 km altitude, and associated with a stratification jump from $N = 10^{-2} \text{ s}^{-1}$ to $N = 2 \times 10^{-2} \text{ s}^{-1}$. An initial low-PV "intrusion" is introduced in the stratosphere together with the active tracer A , of which we investigate the mid-term (tens of days) evolution.

4.1 | Model choice and configuration of the numerical experiments

Tridimensional numerical simulations have been performed with the Advanced Research Weather Research and Forecast (WRF-ARW) model (Skamarock et al., 2008), Version 4.2.2, to investigate the evolution of the diabatically forced vortices. The chosen model is a community model, designed for limited-area simulations of mesoscale flows. It is used operationally for weather forecasting but has been designed so that idealized configurations can also be flexibly used for research (e.g., Bui et al., 2019; Foussard et al., 2019). Two key advantages of this model are its realism and its broad range of uses and hence of validation. It is important to note, however, that there is a significant distance between the degree of idealization considered in the previous section and the flows that can be simulated with WRF, which for instance retains the full complexity of the compressible stratified atmosphere. Choices need to be made for the boundary conditions. In addition, as expected with simulations, the limited resolution will induce numerical diffusion, with significant implications on derived quantities such as PV. Hence, it must be clearly understood that the purpose of these simulations is not to simulate vortices that would reproduce the solutions of the very idealized model or the observations of the previous sections. Rather, they aim at probing, in a more complex and realistic flow, the robustness of features of the theoretical analysis found.

Here, we choose an idealized set-up with open lateral boundary conditions, a free-slip lower boundary condition and a 15 km-deep sponge layer at the top of the 55-km deep domain. Since our primary focus is the idealized simulation of the dry stratospheric flow, no microphysical parameterization is included. The horizontal grid is regular in cartesian coordinate, with the consequence that axisymmetry cannot be strictly conserved. Hence, even in the absence of initial azimuthal perturbation, non-axisymmetric instabilities have the potential to develop and the simulations may be used to assess the stability of the starting axisymmetric flow. The horizontal resolution is 15 km whereas the vertical levels are approximately regularly spaced in altitude corresponding to a vertical resolution of 300 m between 10 and 38 km (the range of altitude of interest). The domain extends from the surface to about 55 km altitude and spans about 3,800 km in the zonal and meridional directions, which amounts to $256 \times 256 \times 161 \approx 10^7$ grid points.

To represent radiative processes acting during the maintenance stage of the plume, we use the simplistic approach consisting in a "heating" (or "cooling") inert tracer but also include a form of radiative damping through Newtonian relaxation. The inert tracer A is introduced in the model as a substitute for radiatively active constituents, such as sunlight-absorbing aerosols (producing heating) or infrared-emitting water vapour (producing cooling). Again, its mixing ratio χ is conserved following the flow, except for numerical and explicit diffusion, and follows Eq. 19 but with this time $\mathcal{D}(\chi)$ standing for an (anisotropic) 3D diffusion operator, which includes both parameterized and numerical contributions. In the default model configuration, a horizontal Smagorinsky first-order closure (Smagorinski, 1963) handles diffusion in the horizontal, whereas in the vertical the constant coefficients of the parameterized second or-

TABLE 1 Table of simulations used in this paper.

name	injection altitude (km)	initial vortex	γ (K/day/(kg/kg)) (per unit tracer mixing ratio)	temperature heating rate $\tau_r = 1/\alpha$ (d)
UP-REF	15	yes	5	7
NO-RELAX	15	yes	5	∞
UP-NOPV	15	no	5	7
DOWN-REF	35	yes	-5	7

der diffusion in altitude coordinate amounts to $0.1 \text{ m}^2/\text{s}$. It should be noted that this relatively simple formulation of diffusion is defined in cartesian geometric coordinate, and the resulting diffusion takes a far more involved form in $R - \theta$ coordinate since R and θ surfaces do not align with r and z surfaces. Newtonian cooling dampens temperature anomalies from the reference temperature profile $\bar{T}(z)$. The full temperature heating rate $\mathcal{H} = T = \frac{T}{\theta} Q$ is of the form:

$$\mathcal{H} = \gamma \chi - \alpha (T - \bar{T}(z)) \quad (21)$$

where γ is the heating (or cooling) rate per unit of tracer mixing ratio and α the temperature relaxation rate. Notice that in our simulation α is uniform and does not depend on the tracer concentration.

Table 1 summarizes the simulations presented in this paper, all on a f-plane and started from an axisymmetric initial state. Different values of γ were tested. In the smoke vortex case (reference simulation), it is chosen to roughly match the observed ascent rate of the Koobor plume (as seen, e.g., in Khaykin et al., 2020) at initialisation. The radiative damping rate is estimated from ERA5 to be on the order of $\alpha = \frac{1}{7} \text{ day}^{-1}$ (Lestrelin et al., 2021).

4.2 | Vortex formation: convective injection

The initialization performed aims at mimicking a redistribution of mass in $R - \theta$ coordinate following Eq. 20. Regarding the amount of material to inject and level of the injection, we have again chosen values inspired by Koobor and take guidance from the ECMWF ERA5 reanalysis on 9 January 2020. Concretely, the initial state in model coordinate is achieved by starting from an atmosphere at rest (i.e., $v = 0$ and $r = R$), in which case μ is also the density in $r - \theta$ coordinate and the corresponding hydrostatic balance equation can be numerically integrating in each model column. In fine, this procedure is equivalent to removing mass from a lower level (the source level) and inserting it at a higher level (the injection level) and represents an instantaneous transfer of mass corresponding to the rapid lifting of air from the lowest layers and its injection into the stratosphere, as may be undertaken by pyroconvection or by the volcanic eruption. The mixing ratio of the active plume tracer A is again initialized based on the correspondence between inverse PV and density in (R, θ) coordinate using Eq. 12. We note again that instead of starting from a fluid at rest and letting the model relax the initial perturbation to reach cyclo-geostrophic balance, a fully balanced structure in (r, z) coordinates could have been diagnosed by imposing both hydrostaticity and cyclo-geostrophy from the initial PV distribution in (R, θ) coordinates, using an approach similar to that of Thorpe (1985). Beyond its simplicity, the present procedure bears several practical as well as fundamental advantages, notably in terms of consistency with the model discretized equations and versatility in the application to more complex background flows, including sheared flows. However, this flexibility comes at some additional computational cost, as small time step integrations are necessary

to correctly resolve the adjustment process.

In the simulations, the unbalanced initial state progressively adjusts while triggering a transient (gravity-wave) response. After a spin-up of about 2 days associated with substantial radiation of gravity waves away from their "convective" source, the f-plane adjustment to this initial mass injection results in the formation of an upper level anticyclone, in agreement with the early theoretical study of extratropical penetrative convection by Shutts et al. (1988). All times in the sequel are defined with respect to a reference at the end of the spin-up.

Figure 5 depicts the balanced state resulting from the injection after the first adjustment period. The adjusted flow is to a very good approximation in gradient wind balance: an elliptical vortex with a wind anomaly ~ 15 m/s is sandwiched between a temperature anomaly dipole of amplitude ± 5 -6 K. The typical size is comparable to that of the vortex displayed on Fig. 2, with the vertical depth $H \approx 4$ km and a diameter $L \approx 1,000$ km. The aspect ratio $\frac{H}{L} \approx 4 \times 10^{-3}$ is close to the value predicted by Charney's quasi-geostrophic scaling ($f/N = 5 \times 10^{-3}$), although the vanishing PV structure lies very far from geostrophy. Another formula proposed by Hassanzadeh et al. (2012); Aubert et al. (2012) suggest that the aspect of an elliptical vortex embedded in a Boussinesq fluid at rest of background Brunt-Väisälä frequency \bar{N} and in gradient wind balance with the environment is:

$$\frac{H}{L} = \frac{1}{2} \left(\frac{f^2 - \zeta_i^2}{\bar{N}^2 - N_i^2} \right)^{\frac{1}{2}} \quad (22)$$

where ζ_i is the vertical component of the absolute vorticity within the vortex and N_i the Brunt-Väisälä frequency inside the vortex. For a low absolute PV vortex ($\zeta_i \approx 0$), Equation 22 can be rewritten:

$$\frac{H}{L} = \frac{f}{2} \left(\frac{g}{T_v} \left(\frac{\partial T'}{\partial z} \right)_v \right)^{-\frac{1}{2}} \quad (23)$$

with $T_v \approx 220$ K the (unperturbed) temperature at the middle of the structure and the lapse rate anomaly $\left(\frac{\partial T'}{\partial z} \right)_v \approx \frac{12}{3.5 \cdot 10^3} \approx 3.4 \times 10^{-3}$ K/m. The value estimated from Eq. 23 is in good agreement with the model. We note that this heuristic formula yields f/N for $N_i = 0$ and $\zeta_i = 0$.

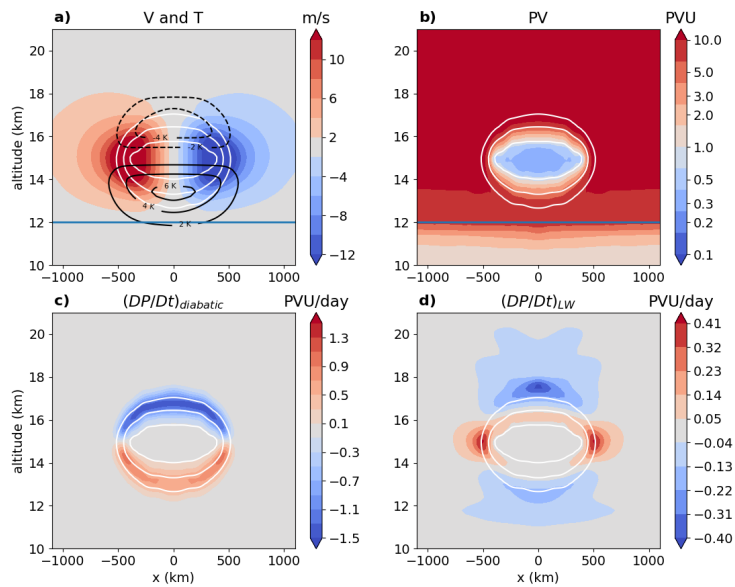


FIGURE 5 Cross-sections of (a) temperature and wind, (b) Ertel's potential vorticity through the adjusted vortex following the injection, (c) Lagrangian PV tendency due to diabatic heating, (d) Lagrangian PV tendency due to the long wave component of heating (UP-REF simulation). White contours are isopleths of tracer mixing A ratio (0.1, 0.5 and 0.9 kg/kg).

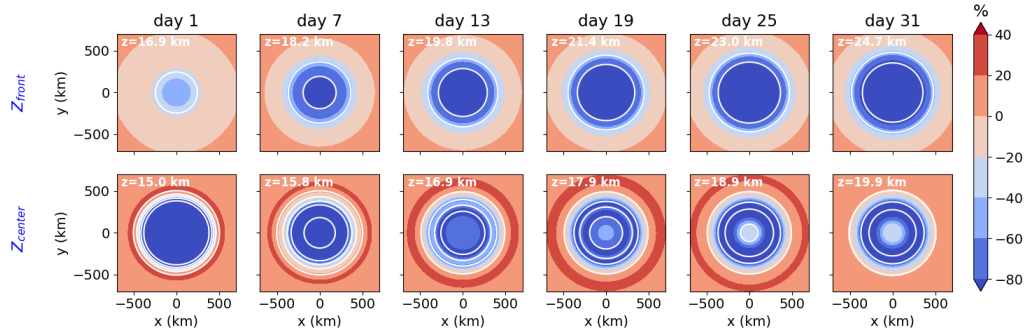


FIGURE 6 Horizontal cross-sections of PV anomaly (colors) and tracer (white contours: 0.1, 0.3, 0.5, 0.7, 0.9 kg/kg) in the reference (UP-REF) simulation, at the level of (top row) the tracer front Z_{front} and (bottom row) the tracer maximum Z_{center} in the UP simulation.

4.3 | Evolution following heating (ascending smoke vortices)

4.3.1 | Evolution in physical space

The configuration described above is run for 40 days after the initial spin-up. Figure 6 displays maps at selected levels exhibiting the evolution of the tracer and PV anomaly, defined as:

$$P_{an} = \frac{P(x, y, \theta, t) - \bar{P}(\theta)}{\bar{P}(\theta)} \quad (24)$$

at the level of the plume core (maximum of χ) and the level of the plume front (maximum of $|d\chi/dz|$). Note that the axisymmetry of the flow is generally preserved over the whole duration of the run. This suggests that the theory from the previous section may be applied, and more generally that vertical cross-sections offer a reliable account of the full dynamics.

Figure 7 depicts such vertical cross-sections for azimuthal wind, temperature anomaly (top row) and relative potential vorticity anomaly (bottom row) through the center of the domain spanning the duration of the simulation. Over the first 12 days of the simulation (first 2 columns in Fig. 7), the core of the low PV and tracer bubble rises by ~ 3 km. Whereas the initially symmetric tracer cloud quickly gains skewness with a steepening of the upper front and a weakening of the gradients in the tail, the PV monopole and the wind and temperature dipoles retain a roughly constant magnitude. This evolution of the dynamical variables, which is related to the persistence of low PV (Eq. 13), is generally compatible with that seen in the ECMWF product (Fig. 2) given the limited vertical resolution of the analysis. We note that there is only limited dilution of the tracer within environmental air. The black contours represent isolines of the potential radius R (i.e., isolines of angular momentum), which are also streamlines of a steadily ascending vortex (see Appendix A1) and here approximately coincide with actual streamlines of the flow (not shown). Those streamlines are deflected around the low PV anomaly, which enables its initial ascent with limited dilution.

Subsequent cross-sections in Fig. 7 reveal that, as time proceeds further, the rising tracer cloud continues to elongate along the vertical direction while keeping an approximately constant horizontal extent. The upper front ascends from ~ 16 to 26 km while the base does not move significantly. This seems broadly consistent with the time evolution of the backscatter ratio observed in Koobor (Fig. 1), with the caveat that backscatter ratio cannot be simply interpreted in terms of aerosol mixing ratio. Whereas the bulk of the tracer remains confined within a strong

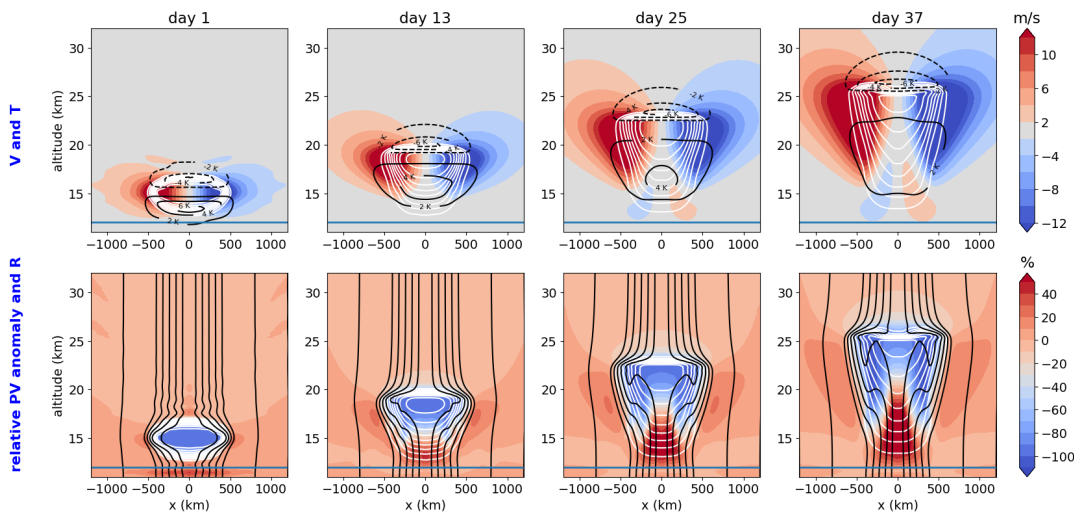


FIGURE 7 Successive cross-sections of (top row) azimuthal wind (colors) and temperature anomaly (black contours) and (bottom row) potential vorticity anomaly from the background (colors) and potential radius R (black contours) for the UP-REF WRF simulation. White contours are isopleths of tracer A mixing ratio (from 0.1 to 1 every 0.1 kg/kg).

anticyclone over the entire duration of the simulation, a weaker cyclone develops at the bottom of the tracer cloud. The positive PV anomaly (cyclonic vorticity) which develops within the tail of the structure gradually deepens and reinforces. The positive-PV appears partly trapped in a shell formed from the downward extension of the low PV upper part. The low-PV region gradually evolves from a vertically symmetric bubble shape to a strongly vertically asymmetric "hollow tooth-shape", characterized by a low PV at the top and lateral edges extending further down about 6 km on day 37. This partly shields the positive PV anomaly, explaining its weaker signature on the wind and temperature fields.

We note that, during its later evolution, the upper part of the structure is the seat of the development of a ring of marginally negative PV, i.e. a region prone to symmetric or centrifugal instability according to the Rayleigh criterion. This potential instability does not however seem to develop into the layered structures expected for centrifugal instability in a stratified fluid (Meunier et al., 2014), at least in the duration of the simulation, and we speculate that this is overwhelmed by the forcing due to the heating. This persistence of the axisymmetry and the limited extension of negative PV areas motivate us to analyze the field in $(R - \theta)$ coordinate.

4.3.2 | Evolution in (R, θ) space

Figure 8 displays the same snapshots of the simulation as in Fig. 7, but with the fields first averaged along the azimuthal direction and transformed to $(R - \theta)$ coordinate. As described above, in that coordinate system, vanishing PV regions collapse to a 1D segment. In $(R - \theta)$, the evolution of the WRF simulation bears striking similarities with the comb of 1D Burgers' equations. This supports the theory presented in Sect. 3.

Neglecting radiative relaxation, according to the demonstration proposed in Sect. 3, the evolution in $(R - \theta)$ may be seen as that of a comb of 1D partial differential equations, with the tracer following a type of Burgers equation and the PV responding to the tracer following Eq. 13. Comparing the full 3D results to the numerical solution to a

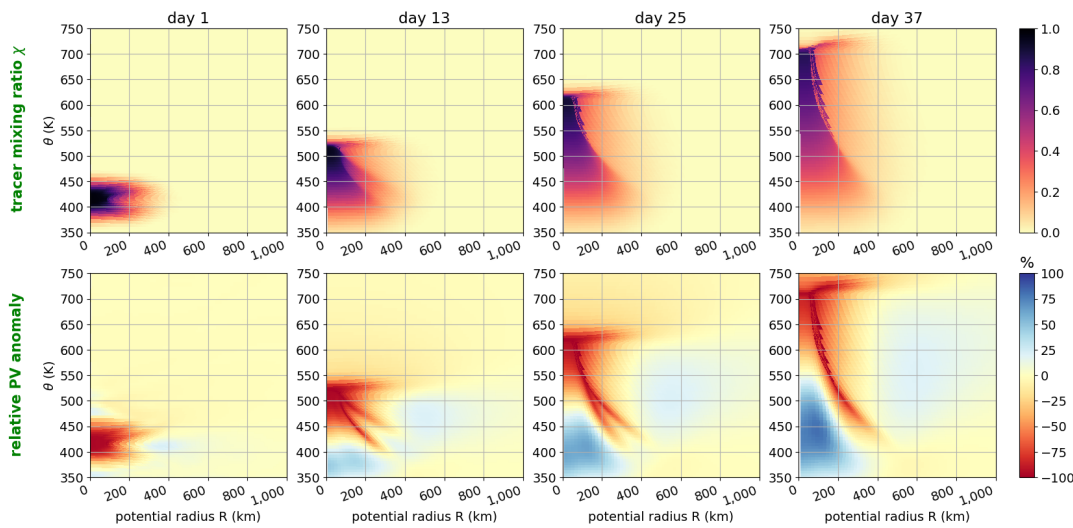


FIGURE 8 Successive cross-sections of (top row) tracer and (bottom row) potential vorticity anomaly from the background in $R - \theta$ coordinate for the UP-REF simulation.

comb of 1-D coupled equations (Eq. (13) and (14)) in Fig. 4, striking similarities are found.

Regarding the tracer, in both cases its dynamics leads to the formation, in each 1D tooth of the comb, of a Burgers-type triangular wave with fronts and tails characteristic of the evolution of a localized maximum (single hump) in Burgers' equation. The varying ascent speeds of the tracer fronts at different potential radii R relate to the initial value of the tracer maximum $\chi_{max}(R)$ (after the adjustment of Eq. (20)) as expected from the Burgers' solution. We note some discrepancy between the theoretical initialization (Eq. 20) and the model field after the initial adjustment (Fig. 8): a homogenization of $\chi_{max}(R)$ along R for $R \leq 100$ km and the generation of two fronts in θ for $100 \text{ km} \leq R \leq 250$ km. Those differences are most likely due to the unavoidable mixing and friction (i.e., diffusion of momentum) occurring during the adjustment and associated cross- R and cross- θ fluxes of PV and tracer. The homogenisation for $R \leq 100$ km is in particular responsible for the straight horizontal front observed at later times (day 25-37) in that range of R in Fig. 8, whereas the double front explains the transient evolution of the tracer (around day 13). Regarding the PV, initially low PV regions of the flow tend to keep their low-PV both in Fig. 4 and Fig. 8, as expected from the maintenance of the initially irrotational flow ($P \approx 0$). Beyond this preservation of the initial condition at short times, the PV dynamics qualitatively evolves towards 0-PV at the tracer front (-100% relative PV anomaly) and a positive PV anomaly in the tail. In the area where there are multiple local maxima along θ , all fronts transiently develop a low-PV anomaly before collapsing into a single one.

Aside from those common features, there are also noticeable differences between the idealized Burgers' solution (Fig. 4) and the WRF simulation. The decrease in the tracer maximum is faster and hence the ascent rate slower in the theoretical solution than in the WRF integration. Whereas both figures highlight a PV dipole, the negative PV anomaly quickly (15 days) collapses onto the front in the case of the Burgers' solution but remains spread out around the front in the 3D WRF simulation. The respective role of radiative damping and diffusion in shaping those differences will be discussed in Sect. 5.

4.4 | Evolution following cooling (descending water-rich/ozone-poor plumes)

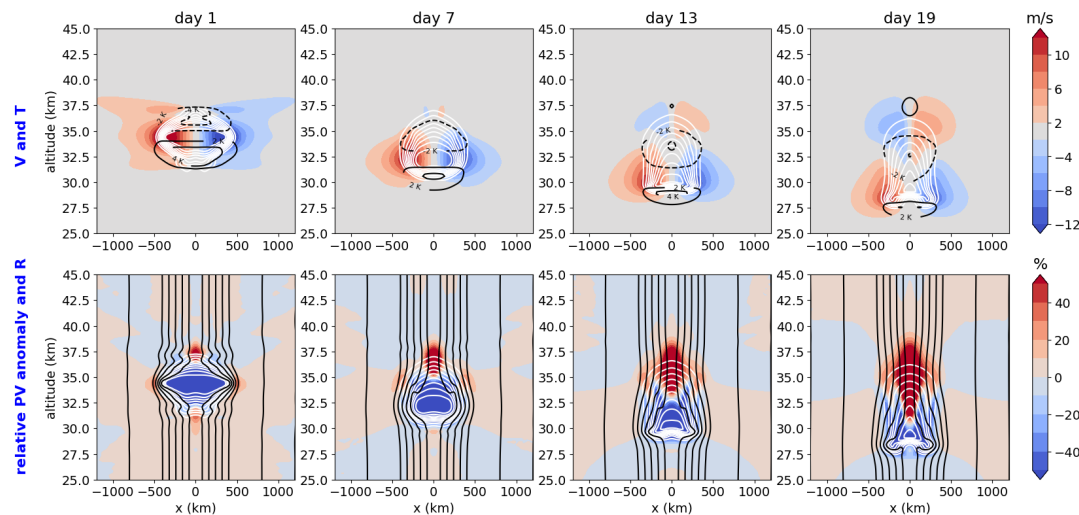


FIGURE 9 Successive cross-sections of (top row) wind (colors) and temperature anomaly (black contours) and (bottom row) potential vorticity anomaly from the background (colors) and momentum radius R (black contours) for the DOWN-REF simulation. White contours are isopeths of A tracer mixing ratio (from 0.1 to 1 every 0.1 kg/kg).

Up to now, we have been focusing on the case of a heating tracer, which was motivated by observations of stratospheric wildfire plumes. A volcanic plume reaching deep in the stratosphere is expected to detrain large amounts of water vapor, as anticipated early on (e.g. Glaze et al., 1997) and recently observed in the aftermath of the January 2022 Hunga Tonga-Hunga Ha'apai (HTHH) eruption (Millán et al., 2022; Khaykin et al., 2022a). Following the latter event, Sellitto et al. (2022) suggested that radiative cooling from the injected water vapor is likely to strongly dominate the diabatic forcing. Indeed, evidence of compact descending patches of volcanic compounds in the HTHH plume was shown in Legras et al. (2022). Motivated by this natural example, we explore the response of the stratospheric flow to a cooled tracer bubble. Contrary to the previous subsection, however, we do not aim here at a direct comparison with a natural event. Rather, we consider the idealized case of a cooling tracer injected in the midlatitude stratosphere at 35 km altitude. The cooling rate per unit tracer is now $\gamma = -5$ K/day/(kg/kg), i.e. opposite to the heated case. We note that such magnitude of the cooling remains within the range of plausible values; for instance, Sellitto et al. (2022) estimated the cooling rate in the HTHH plume to be on the order of $T = -10$ K/day at the day +3 stage.

Even faster than in the ascending case, the initial anticyclonic 'bubble' structure gradually breaks and a cyclonic vortex develops within the tail of the tracer cloud. Overall, the qualitative evolution is again consistent with Eq. 16, with lower relative PV anomaly at the location of the tracer front and a trapping of the tracer within an anticyclone. However, whereas in the heated tracer the dominant signature was that of the anticyclone, here it is the cyclonic circulation in the tail. This occurs as a consequence of the background PV gradient.

Figure 10 depicts the same pattern in (R, θ) coordinate. Again, the time evolution features fronts and tail although in an opposite direction compared with the ascending vortex. A fundamental difference with the ascending case is the orientation of the motion with respect to the background PV gradient. This results in the larger dilution of the tracer in denser air in (R, θ) space (Eq. 14) and its contraction in physical space. Due to its advection in a lower

PV environment, the magnitude of the anticyclonic PV anomaly reduces over time whereas that of the positive PV anomaly grows. This evolution is generally opposite to the ascending case.

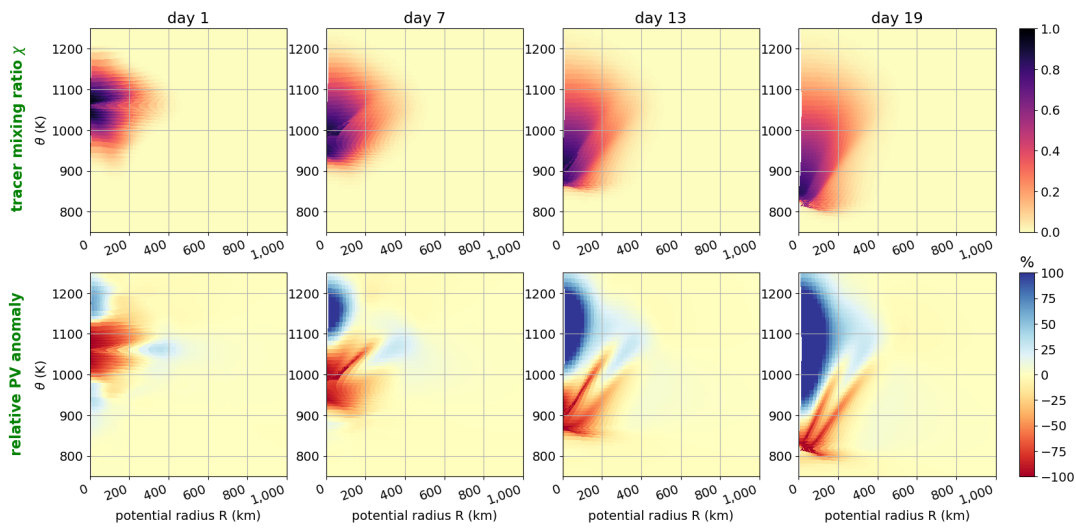


FIGURE 10 Successive cross-sections of (top row) tracer and (bottom row) potential vorticity anomaly with respect to the background in $R - \theta$ coordinate for the DOWN-REF simulation.

Peer Review

5 | DISCUSSION

5.1 | Roles of radiative relaxation and friction

The comparison between Burgers' solution and the 3D simulations revealed striking agreement on key qualitative features. It has also highlighted significant differences. The magnitude of the PV anomalies in the Burgers solution (Fig. 4) largely exceed those in the 3D WRF simulation. Indeed, the PV anomaly in UP-REF extends over a broader range of θ and is less intense while the positive anomaly in the tail is weaker. We expect that such discrepancy partly results from the missing radiative relaxation in the derivation of the equivalent Burgers equation. The effect is illustrated in Fig. 5 (panel d), which shows that, by redistributing heating over a deeper layer, the radiative relaxation tends to induce a significant negative PV tendency extending above and below the plume, beyond the area where the tracer lies, broadening the sharp PV tendency induced by the tracer only. We also note that the larger positive PV anomalies appear more damped than negative PV anomalies, which is a consequence of the maintenance of low PV. Qualitatively, we expect that this deeper heating tends to slow down the sharpening of the tracer front and to partly shield the tracer cloud and limit dilution.

To assess the impact of radiative relaxation within the theoretical framework, we attempted to move beyond Burgers type solution and include the additional heating term in a new numerical model solving Equations (13) and (14). This new model requires inverting the temperature anomaly distribution from the PV field to compute thermal relaxation; for internal consistency, this is achieved without any information from the WRF simulation but instead using a quasi-geostrophic (QG) ansatz and assuming a typical horizontal scale λ_h ($\lambda_h = 250$ km) of the structure. The model also includes explicit diffusion in the PV equation. A full description of the 1D model, including the QG temperature anomaly inversion, is provided in Appendix A3. For quantitative comparison, it is initialized from the axial profile of tracer and PV of the WRF simulation after the 2-day spin-up.

Sensitivity calculations in this 1D framework confirm that increasing the temperature relaxation rate α slows down the decay of the maximum tracer mixing ratio and therefore increases the vertical ascent rate of the front, although without preventing its formation. Decreasing the horizontal scale $\frac{1}{\lambda_h}$ reduces the amplitude of the temperature anomaly and shallows its vertical scale. While we restricted ourselves to a range of diffusivities K low enough such that diffusion only marginally affects the results (in particular the decay of the tracer maximum or its propagation speed remain insensitive to this parameter), this term still controls the width of the tracer front. Figure 11 compares the evolution of the tracer, PV and temperature profiles in the WRF UP-REF simulation with integrations of the 1-D model for an adjusted set of parameters ($\gamma = 5$ K/day/(kg/kg), $1/\alpha = 5$ days, $K = 17$ K²/day, $1/\ell = 250$ km, see Appendix A3). There is a fair agreement for the tracer with a triangular wave characterized by similar peak value. The distribution of PV also depicts a relatively good agreement between the two approaches, from shorter times, when the low PV cloud is preserved, to longer times in particular regarding the sharpness of the minimum PV located at the front. The PV jump behind the front is larger in the 1-D model which is not contaminated by lateral cross-R fluxes.

Another discrepancy with the WRF simulation lies in the evolution of the amplitude of the negative temperature anomaly. While decaying with time in the 1D model (by a factor of 2 over the course of the integration), it remains rather stable and even tends to grow over most of the WRF simulation. This may be related to the assumption of a constant horizontal scale λ_h in the QG inversion. The 3-D simulation (Fig. 7) actually shows a lateral expansion of the anticyclone with time and increasing λ_h would indeed increase the amplitude of temperature anomaly. This decrease of the temperature anomaly above the front is the likely reason to explain the need of an increased value of α in the 1-D model.

In order to further confirm the effect of radiative relaxation, we performed another WRF numerical experiment

with Newtonian relaxation switched off (not shown). The early development shows a qualitatively similar general evolution, but a significantly shallower area of negative PV anomaly and an enhanced dilution of the tracer, in agreement with theoretical expectations. At later stages, this smaller tracer mixing ratio leads to a slower ascent, in agreement with the effect of the α parameter in the 1-D model. This points to an important role of the longwave radiative heating in the dynamical evolution of the anticyclone. Here, we only included a simplistic parameterization of radiative relaxation with uniform damping parameter, which only accounts for the temperature anomaly. The impact of the complex mixture of compounds radiatively active in the infrared contained in wildfire plumes, including both black carbon aerosols and greenhouse gases (water vapor, carbon monoxide, etc.), remains to be assessed.

Besides radiative relaxation, some differences between the theory and the WRF simulation must be a consequence of the diffusion of momentum generating a cross-R flow. In particular, in the 3-D simulation, the top of the tracer front exhibits a protrusion towards large R . It corresponds to the tracer ring topping over the plume (seen in Fig. 7). Such feature cannot occur from an inviscid evolution from the initial condition. We interpret this protrusion as resulting from drag occurring at the top of the vortical flow where the vertical derivative of the balanced azimuthal wind is largest leading to positive $R = \frac{r}{R} F_{\lambda}$. As a proxy for friction, we examined the repartition of regions of low Richardson number (not shown), which indeed emphasize both the shallow front and lateral tail of the tracer cloud as regions with significant likely significant turbulence/mixing. The global impact of friction may also be grasped by considering the integral of Eq. 10 along θ : only friction can result in mass fluxes across R-isocontours. This is shown in Fig. 8 (bottom row) for both the mass of air and tracer. During the course of the simulation, the mass of air enclosed within $R < 100$ km and $360 \text{ K} < \theta < 800 \text{ K}$ is reduced by 30%, demonstrating significant viscous drag effects which are not captured in the 1D- framework. This effect is enhanced when the flux of tracer A is considered, emphasizing that the exchange of mass through friction is either located in regions of high tracer content or the existence of cross-R diffusion of A . Overall, this suggests a significant role of dynamic instabilities and associated drag in the evolution of anticyclonic plumes, an effect which cannot be accounted for in a purely 1D framework.

5.2 | Mixing of the plume with environmental air: impact of low PV initialisation

A special property of the vertically moving plumes is their sustained isolation from the environment, which occurs along both horizontal and vertical motions. At this scale, it might have been expected that the radiative instability driven by the heating results in significant mixing between the plume and the environment. We have seen that this is not the case, for two reasons. First, the presence of a low PV anomaly is associated with streamlines avoiding the tracer cloud, thus preventing its dilution within background stratospheric air. Second, as argued above, the additional heating provided by the longwave relaxation of the temperature perturbation induced by the PV anomaly reduces dilution within outside air. The overarching effect is to stabilize the structure. In the absence of an initial PV anomaly, there is no temperature anomaly and this shielding is absent.

Thus, it is expected that the co-injection of absorbing tracer and 'air' mass, resulting in a plume initially trapped within a vanishing absolute PV anticyclone plays a key role in preventing dilution of the absorber along the ascent through the effect of both dynamical isolation in 0-PV air and thermal relaxation. This initial PV anomaly may have been considered as a necessary condition for the formation of the anticyclone, but a few previous studies (e.g. Doglioni et al., 2022) achieved to simulate a vortex by adding absorbing aerosol while ignoring the direct dynamical impact of the injection on the dynamics in high resolution simulations. More recently, the coarse-resolution (200 km) simulations by Senf et al. (2023) did not simulate the vortex. In order to test the impact of the injection in shaping the plume evolution, we performed a simulation including the same initial aerosol profile but without the mass injection (i.e. from a fluid with no PV perturbation, simulation UP-NOPV). As shown in Fig. 12, an anticyclone forms at the level

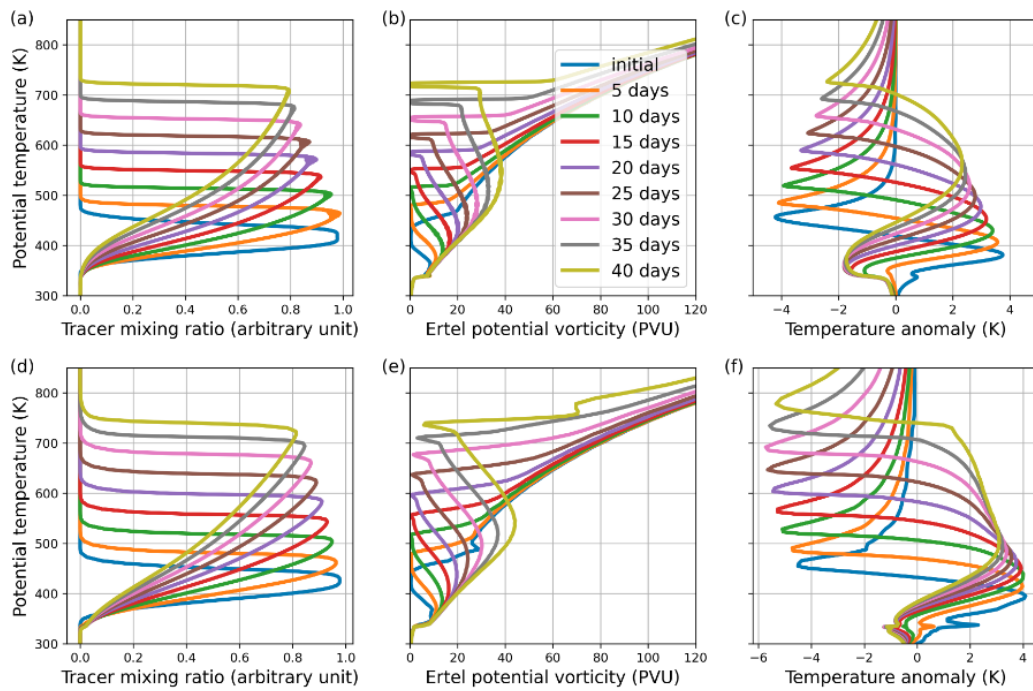


FIGURE 11 Profiles of (a, d) tracer mixing ratio, (b, e) potential vorticity and (c, f) temperature anomaly. Panels (a), (b), (c) correspond to numerical integration of Eqs.(13) and (14) with the diabatic heating defined by Eq. 21 and the temperature inverted using the formula provided in Appendix A3 with $1/\ell = 250$ km. Panels (d), (e) and (f) are average profiles for $0 \leq R \leq 60$ km in the reference simulation.

of the tracer front. However, it only encompasses a small fraction of the tracer plume after 2 weeks of simulations. Second, the dilution of the tracer is larger and, contrary to the case with a co-injection of mass, the initial axisymmetry of the plume is not maintained. On the contrary, we observe a destabilization of the initially axisymmetric flow. Whereas there seems to be a relaxation towards axisymmetry at later times, the anticyclonic plume trapping is still weak on day 19 of the simulation.

Such long-term difference between the case with and without initial mass injection is reduced when we consider an absorbing tracer injection below the tropopause, between 10 and 12 km, as used by Doglioni et al. (2022) (not shown). Although a breaking of the axisymmetry of the flow still occurs in the absence of mass injection, the significant and distinct PV anomalies created by the diabatic tropopause crossing tend to more rapidly merge (within less than two weeks, not shown).

In realistic dynamical settings, the initial concomitance of absorbing tracer and low PV anomalies is expected to play an essential role in the rapid formation of a compact plume both below and above the tropopause. We speculate that the PV signature will favor the emergence of a single coherent plume from a number of low PV patches through vortex merger (e.g., Dritschel, 2002; Reinaud and Dritschel, 2002). In the case of the Australian fires, several (about ten) large pyrocumulonimbii reached the stratosphere (Peterson et al., 2021) and probably later self-organized into a small number of vortices, including Koobor. As discussed above, the PV anomaly also prevents the fast initial dispersion of the tracer which would otherwise arise due to vertical shear and large-scale horizontal deformation by the flow.

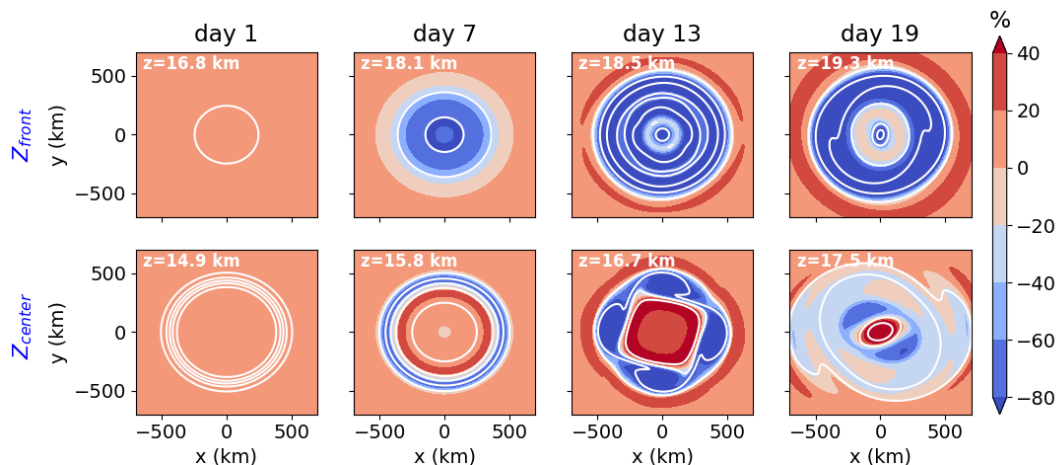


FIGURE 12 Horizontal cross-sections of PV anomaly P_{an} (colors) and tracer (white contours: 0.1, 0.3, 0.5, 0.7, 0.9 kg/kg) in the UP-NOPV simulation, at the level of (top row) the tracer front and (bottom row) the tracer maximum in the UP simulation.

5.3 | Environmental conditions for anticyclonic plume formation: altitude and latitude of the injection

In our conceptual model, the (cross-isentropic) injection of mass near the level of neutral buoyancy is sole responsible for the initial formation of the vortex. From a dynamical point of view, the vertical gradient of potential vorticity or the difference between tropospheric and stratospheric PV do not play any direct role, since Lagrangian conservation of PV does not apply.

However, for a similar amount of injected mass, the smaller the background isentropic density σ , the larger the relative PV anomaly. Given the background profile of σ , it comes with no surprise that anticyclonic plumes are more likely to occur higher in the atmosphere where the fluid is lighter and more stratified. This effect is further reinforced when considering the absolute PV anomaly, and partly explains why this phenomenon, which is key in the extratropical stratosphere, was not reported after diabatic tropospheric injections.

A second important factor is the latitude of the injection, upon which the Coriolis parameter f depends. So far, we completely ignored this factor by adopting the f -plane approximation. In particular, the strength of the anticyclonic trapping may be crudely evaluated by comparing the magnitude of the relative vorticity (f) to the change in planetary vorticity between the center and the edge of the structure. In polar and midlatitude regions, a quasi-0 PV is extremely rare around and provides strong isolation. In contrast, in tropical regions, ambient PV is closer to 0 and the low PV vortex formation and isolation is limited.

The adimensional number comparing latitudinal vorticity variations to the magnitude of the local vorticity anomaly ($\approx -f$ in a 0-PV vortex) is $\frac{L}{f\beta}$ where $\beta = \frac{2\Omega}{a} \cos(\phi)$ ($a = 6,400$ km is the planetary radius, ϕ the latitude and $\Omega \approx 7.27 \cdot 10^{-5} \text{ s}^{-1}$ the Earth rotation rate) and L is the horizontal scale of the vortex. Assuming that the typical horizontal size of the structure L is on the order of the Rossby radius of deformation radius R_d , as suggested by its aspect ratio, $\frac{L}{f\beta} = \frac{\beta R_d}{f} = \frac{\beta NH}{f^2} = \frac{NH}{2\Omega a \sin \phi \tan \phi}$. For an injection of depth $H \approx 1$ km in the stratosphere ($N \approx 2 \cdot 10^2 \text{ s}^{-1}$), the condition $\frac{\beta L}{f} > 5 \gg 1$ is satisfied poleward of about 20° and such injections will result in trapping. At latitudes closer to the equator ($\frac{L}{f\beta} \gg 1$), the efficiency of the trapping is reduced as the latitude shift necessary to reach a similarly

low PV on an isentropic surface diminishes. Hence, in tropical regions, trapping is weaker - provided it occurs. The dynamical response to heating is affected by the equatorial beta effect, as suggested for the evolution of the HTHH plume by Schoeberl et al. (2023). We leave investigations of this interesting aspect to future dedicated studies.

6 | CONCLUSION

Diabatically-forced anticyclonic plumes in the stratosphere were discovered in 2020. Following the extreme 2020 Australian wildfires, a radiatively heated vortex was observed to ascend from 18 to 35 km in the stratosphere. The plume of the 2022 Hunga Tonga-Hunga Ha'apai eruption underwent a spectacular diabatic descent due to the cooling by an extreme water vapor anomaly. By hindering the dilution of the plume, vortical structures largely modify its longevity and impact on radiation, chemistry and dynamics. From the point of view of geophysical fluid dynamics, those objects exhibit several peculiarities, in particular a virtually-0 potential vorticity at their center according to the ECMWF reanalysis. Such conditions are rarely met in the midlatitude stratosphere apart from tropical intrusions.

Here, we adapted a theoretical framework developed for tropical cyclones (Schubert and Alworth, 1987) to study the dynamics of potential vorticity in diabatically-forced axisymmetric anticyclones on the f -plane. As a consequence of the mathematical definition of PV, an extension of the impermeability theorem of Haynes and McIntyre (1987) holds, which states that the PV substance (the PV multiplied by the mass of air) is constant within a control volume delimited by constant angular momentum-potential temperature surfaces (R, θ) . This property offers a clear picture of the initial formation of stratospheric anticyclonic plumes: the direct injection of mass in the stratosphere by pyroconvection or volcanic eruption is associated with a dilution of the PV substance and a decrease of PV. In reality, the initial formation stage may additionally imply vortex merger of a number of distinct initial injections. If the total amount of injected mass is sufficiently large compared to the background, the PV substance is extremely diluted and the PV approaches zero.

The subsequent evolution of the vortex is controlled by radiative heating or cooling within the plume. At first order, the radiative effect of the sunlight-absorbing aerosols or infrared-emitting water vapor can be idealized by introducing an radiatively active but chemically inert tracer A which heats or cools the air at a rate proportional to its mixing ratio. If the active tracer is trapped within an exactly 0-PV bubble, as may approximately occur following the injection, the heated or cooled balanced vortex plume is an exact solution of the governing dynamical equations. Thus, the observation of near 0-PV is anything but incidental, and fundamental to the preservation of the structures against dilution as they move vertically through the stratosphere.

Reasonably, no mass injection is large enough to completely overcome the background mass distribution, and low PV, rather than a strictly 0-PV, has to be considered. This new problem, complex in standard cylindrical coordinates, is again greatly simplified in angular momentum-potential temperature coordinates. Then, as long as radiative relaxation of the induced-temperature anomaly remains significantly smaller than direct heating by the tracer, the diabatic motion of the active tracer reduces to a variant of Burgers' equations whereas PV passively follows the tracer evolution. Such Burgers-style dynamics leads to the formation of a tracer front upstream of the vortex relative to its motion (top for heated, bottom for cooled vortices), as observed in CALIOP particulate backscatter for the Australian vortices. Near the front, mass converges and low PV is sustained. On the contrary, the downstream part of the vortex features a tail with reduced tracer gradients, mass divergence and generation of cyclonic PV. At first order, this conceptual picture is validated by numerical simulations performed with the Weather Research and Forecast model. In particular, the cyclonic PV anomaly, which is not discernable in the ECMWF ERA5 reanalysis, emerges in the later part the simulation, although it appears shielded by negative PV and has a radial extent reduced compared to the anticyclonic

PV. Compared to the inviscid theory, the simulations also emphasize the role of diffusion of momentum, secondary in the beginning but significant in shaping the long-term evolution of the structure. In theory, friction can be directly quantified in (R, θ) and this aspect deserves dedicated investigations.

Several key processes were ignored in our set-up. Notably, vertical shear of the horizontal wind may be an important player in the evacuation of the cyclonic tail and the maintenance of the ellipsoidal shape of the anticyclone. Variations of the Coriolis parameter will become central in the latitudinal drift of the anticyclone or the evolution of tropical plumes. Other crude simplifications concern the radiation and, for absorbing particles, aerosol microphysics. The parameterized radiative heating/cooling rate did not vary in time, and more importantly, depends linearly on the tracer mixing ratio. While we do not expect that diurnal variations of the heating will have a strong impact on the overall-balanced plume, non linearities in the heating function (e.g. saturation above a given tracer concentration) could strongly affect the dynamics. Regarding microphysics, the vertical motion of the tracer was assumed purely Lagrangian, which is well-adapted to gases but fails to describe particles over the course of 3 months if they undergo even weak sedimentation relative to the flow. The respective role of those different processes should be assessed in future works. Extreme wildfires are expected to become more frequent in the coming decades due to climate change. Meanwhile, there are important stakes around understanding volcanic perturbations of the stratospheric aerosol layer due to the need to assess the potential effects and likely risks of stratospheric geoengineering. In this context, it is crucial to better constrain the dynamical behavior of stratospheric volcanic and wildfire plumes as a prerequisite to reliably quantifying their long-term impact on ozone chemistry, stratospheric circulation and global climate.

Peer Review

A1 | APPENDIX: THE UNIFORMLY HEATED (OR COOLED) 0-PV BUBBLE, AN EXACT VERTICALLY TRAVELLING SOLUTION

Given the absence of interaction between the outside air in the case of a 0-PV frictionless flow, a natural question which arises is the existence of vertically traveling solutions conserving their shape. We will now illustrate that they do exist for a variety of geometric configurations of the bubble and background, in the case of the frictionless Eliassen balanced vortex model under anelastic approximation. The solutions require that the PV is strictly 0 and are considered for a heating Q function only of the tracer content.

Potential vorticity is given in Eq. 3. For the sake of completeness, the governing equations are provided hereafter. The horizontal momentum equations in cylindrical (r, λ, z) coordinate, assuming no azimuthal dependency ($\partial_{\lambda} \dots = 0$) read:

$$\begin{aligned} \frac{Du}{Dt} - \left(f + \frac{v}{r}\right)v &= -\frac{\partial\phi}{\partial r} \\ \frac{Dv}{Dt} + \left(f + \frac{v}{r}\right)u &= F_{\lambda} \end{aligned} \quad (\text{A1})$$

where ϕ is the geopotential and $\frac{D}{Dt} = \frac{\partial}{\partial t} + u\frac{\partial}{\partial r}$. Note that we only retained the component of the mechanical forcing along the azimuthal direction (in other words, $\mathbf{F} = (F_{\lambda}, 0, 0)$). In the Eliassen balanced vortex model (Eliassen, 1952; Schubert and Hack, 1983), the azimuthal flow is cyclogeostrophically balanced (the radial momentum equation reduces to $(f + \frac{v}{r})v = \frac{\partial\phi}{\partial r}$) and may be diagnosed from the knowledge of the PV distribution in (R, θ) , making use of the gradient wind equation. However, as detailed below, its exact shape and the nature of the balanced flow does not affect our discussion.

The potential temperature equation reads:

$$\frac{D\theta}{Dt} = Q \quad (\text{A2})$$

and the tracer mixing ratio equation in:

$$\frac{D\chi}{Dt} = 0 \quad (\text{A3})$$

Making the anelastic approximation, the continuity equation in cylindrical coordinates is:

$$\frac{1}{r} \frac{\partial ru}{\partial r} + \frac{1}{\rho_0} \frac{\partial \rho_0 w}{\partial z} = 0 \quad (\text{A4})$$

The question we ask concerns the existence of vertically moving solutions of the Eliassen equations without change of shape. It is, in essence, similar to the problem of a solid body ascending in a perfect fluid, since there should be no mixing with the environment. It is a classical problem of fluid mechanics (e.g. Taylor, 1922), and we refer the reader to the general resolution method by Long (1953). Let us write W the rate of ascent/descent. The anelastic Stokes stream function in the moving frame reads ascending vertically at a speed W :

$$(\rho_0 u, \rho_0 (w - W)) = \left(-\frac{1}{r} \frac{\partial \Psi}{\partial z}, \frac{1}{r} \frac{\partial \Psi}{\partial r} \right) \quad (\text{A5})$$

The equations of conservation of R^2 , θ and P can be rewritten:

$$\frac{\partial R^2}{\partial t} + \frac{1}{\rho_0 r} \left(\frac{\partial(\Psi, R^2)}{\partial(r, z)} \right) + W \frac{\partial R^2}{\partial z} = 0, \quad (\text{A6})$$

$$\frac{\partial \chi}{\partial t} + \frac{1}{\rho_0 r} \left(\frac{\partial(\Psi, \chi)}{\partial(r, z)} \right) + W \frac{\partial \chi}{\partial z} = 0, \quad (\text{A7})$$

$$\frac{\partial \theta}{\partial t} + \frac{1}{\rho_0 r} \left(\frac{\partial(\Psi, \theta)}{\partial(r, z)} \right) + W \frac{\partial \theta}{\partial z} = Q, \quad (\text{A8})$$

$$\frac{\partial P}{\partial t} + \frac{1}{\rho_0 r} \left(\frac{\partial(\Psi, P)}{\partial(r, z)} \right) + W \frac{\partial P}{\partial z} = \frac{1}{\rho} \zeta_a \cdot \nabla Q, \quad (\text{A9})$$

$$(\text{A10})$$

The condition for the existence of stationary ascending structures in the moving frame are: $\frac{\partial R^2}{\partial t} = -W \frac{\partial R^2}{\partial z}$, $\frac{\partial(\theta - \bar{\theta})}{\partial t} = -W \frac{\partial(\theta - \bar{\theta}(z))}{\partial z}$, $\frac{\partial \chi}{\partial t} = -W \frac{\partial \chi}{\partial z}$ and $\frac{\partial P}{\partial t} = -W \frac{\partial P}{\partial z}$. Injecting this form of the time derivative into the equations yields:

$$\frac{1}{\rho_0 r} \left(\frac{\partial(\Psi, R^2)}{\partial(r, z)} \right) = 0, \quad (\text{A11})$$

$$\frac{1}{\rho_0 r} \left(\frac{\partial(\Psi, \chi)}{\partial(r, z)} \right) = 0, \quad (\text{A12})$$

$$\frac{1}{\rho_0 r} \left(\frac{\partial(\Psi, \theta)}{\partial(r, z)} \right) = Q - W \frac{d\bar{\theta}}{dz}, \quad (\text{A13})$$

$$\frac{1}{\rho_0 r} \left(\frac{\partial(\Psi, P)}{\partial(r, z)} \right) = \frac{1}{\rho} \zeta_a \cdot \nabla Q, \quad (\text{A14})$$

In this stationary translation, isolines of χ and R are both streamlines and parallel to one another. Hence, the only possibility that a localized tracer patch (i.e. satisfying $\chi = 0$ a finite distance away from the patch center) exists (given the geometry of R) is that it lies within a closed R^2 contour, i.e. an area where $\nabla R^2 = 0$ (and hence $P = 0$).

Let us now consider the case of patches of $P = 0$ containing the tracer with constant concentration $\chi = 1$ and hence $Q = \gamma$, embedded within a background of uniform PV $P = \bar{P} > 0$ and $\chi = 0 = Q$. Outside of the $P = 0$ patches, $\nabla R^2 \neq 0$ and the streamfunction may be written as a function h of R^2 , i.e. $\Psi = h(R^2)$.

In this configuration, Equation A14 is identically verified both outside and within the area where the tracer lies, with $\nabla Q = 0$ (since Q a function of χ and χ uniform) and $\frac{\partial P}{\partial r} = \frac{\partial \bar{P}}{\partial z} = 0$ (since P uniform). Similarly, Equation A13 also holds as long as: $Q = W \frac{d\bar{\theta}}{dz}$, θ is a function h of Ψ inside the patch and $h'(R^2) = -\frac{Wf}{2\bar{P}} \frac{d\bar{\theta}}{dz}$.

Indeed, outside the patches, we have $Q = 0$ and, making use of the form of the streamfunction $\Psi = h(R^2)$, the constraint in Equation A13 is equivalent to :

$$\frac{1}{r\rho_0} h'(R^2) \left(\frac{\partial(R^2, \theta)}{\partial(r, z)} \right) = -W \frac{d\bar{\theta}}{dz} \quad (\text{A15})$$

which may be identified to the (constant) environmental PV \bar{P} :

$$\frac{1}{r\rho_0} \left(\frac{\partial(R^2, \theta)}{\partial(r, z)} \right) = \frac{2\bar{P}}{f} \quad (\text{A16})$$

with $h'(R^2) = -\frac{Wf}{2\bar{P}} \frac{d\bar{\theta}}{dz}$. Inside the patch, similar considerations show that $Q = W \frac{d\bar{\theta}}{dz}$ (and θ function of Ψ).

This little exercise demonstrates that $P = 0$ patches constantly heated by a Lagrangian tracer embedded in a tracer-free constant PV background flow are travelling solutions of the axisymmetric Eliassen balanced vortex equations. This result holds for an isolated vortex, but also for heated/cooled vorticity rings. Furthermore, its derivation relies solely on the definition of PV. The balance equations only intervene as an additional constraint needed for the determination of the vortical flow. In cylindrical geometry, the solution to this problem involves solving a non-linear elliptic equation (Thorpe, 1985) which complicates analytical explorations. However, we note that the translation property of $P = 0$ patches follows from the very definition of PV in a 2-D flow and is also valid in 2-dimension cartesian geometry (i.e. with plane symmetry). In this case, there exist analytical solutions of the balanced flow induced by a PV anomaly (Gill, 1981) which may offer a path towards analytical tractability.

An interesting (though expected) consequence is that contours of R^2 are streamlines of the ascending/descending heated/cooled 0-PV structure, which was emphasized in Taylor (1922); Long (1953). Thus, upon closer inspection, it turns out that the conceptual model proposed by Lestrelin et al. (2021), namely a vanishing PV ascending vortex, still holds in the sense of the Eliassen balanced vortex including diabatic forcing. The solution remains highly idealized and it is not clear how the flow will evolve in the presence of friction and tracer diffusion to non zero PV areas. This is next explored by the means of idealized simulations.

A2 | APPENDIX : FRONTAL PV DYNAMICS

This appendix examines the role of frontal tracer dynamics in the creation of anticyclonic potential vorticity. Let us parameterize mixing as $\mathcal{D} = K \partial_{\theta}^2$ with constant diffusivity $K > 0$. Equation 19 is now the viscous Burgers' equation. It admits as an analytical solution the steadily propagating front, which may be written:

$$\chi(\theta, t) = \frac{\chi_{max}}{2} (1 - \tanh(\xi)) \quad (\text{A17})$$

with

$$\xi = \frac{\gamma \chi_{max}}{4K} \left(\theta - \frac{\chi_{max}}{2} \gamma t \right) + a$$

where χ_{max} is the tracer maximum (height of the front) and a an arbitrary integration constant. Here, the front has width $K(\gamma \chi_{max})$ and it is traveling at speed $\gamma \chi_{max}/2$. Assuming the tracer profile from Eq. A17, the hyperbolic PV equation 13 may be solved along its characteristics (here, material trajectories) for each value ξ_0 . Lagrangian variations of ξ are governed by the ordinary differential equation:

$$\frac{D\xi}{Dt} = -\frac{(\gamma \chi_{max})^2}{(8K)} \tanh(\xi) \quad (\text{A18})$$

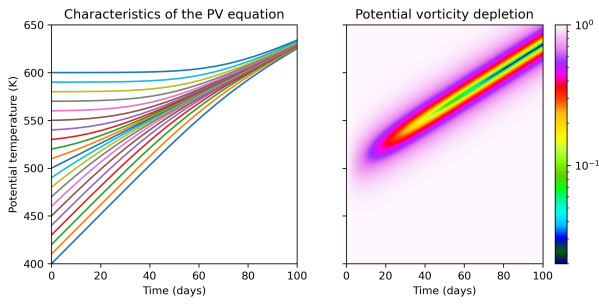


FIGURE A1 (a) Characteristics of the potential vorticity equation for $\gamma = 5 \text{ K/day}/(\text{kg/kg})$, $K = 17 \text{ K}^2/\text{day}$, $\chi_{max} = 1$ and a front initially at $\theta_0 = 500 \text{ K}$. (b) Evolution of the potential vorticity ratio P/P_0 for these conditions.

which integrates in $\sinh \xi = \sinh \xi_0 \exp\left(\frac{(\gamma \chi_{max})^2 \tau}{8K}\right)$, yielding the characteristics. Injecting into the expression of $Q_\theta = \gamma \chi_\theta$ and using the solution to Eq. (13) along its characteristics, we obtain the parametric solution:

$$\theta(\xi_0, t) = \frac{4K}{\gamma \chi_{max}} \left(\frac{\chi_{max}^2 \gamma^2 t}{8K} + \operatorname{arcsinh} \left[e^{-\frac{\chi_{max}^2 \gamma^2 t}{8K}} \sinh \xi_0 \right] - a \right), \quad (\text{A19})$$

$$P(\theta(\xi_0, t), t) = P_0(\theta(\xi_0, 0)) \sqrt{\frac{1 + \sinh^2(\xi_0)}{e^{\frac{\chi_{max}^2 \gamma^2 t}{4K}} + \sinh^2(\xi_0)}}. \quad (\text{A20})$$

As shown in Fig. A1, the characteristics gather in the frontal region of the tracer distribution due to the advective effect of the heating and (A20) demonstrates that PV decays exponentially to zero but without a finite time singularity unlike the case of a non diffusive tracer, even without dissipation in the PV equation.

A3 | APPENDIX : COUPLED TRACER-PV 1D MODEL INCLUDING THERMAL RELAXATION

In order to assess the role of radiative relaxation, we built a 1D model solving the coupled Eq. (13) for the PV and Eq. (14) for the tracer, with a diffusion: defined by:

$$\frac{\partial \chi}{\partial t} + Q \frac{\partial \chi}{\partial \theta} = \frac{1}{\bar{\mu}} \frac{\partial}{\partial \theta} \left(K \bar{\mu} \frac{\partial \chi}{\partial \theta} \right) \quad (\text{A21})$$

In practice, the diffusivity for the tracer is $K = 17 \text{ K}^2 \text{ day}^{-1}$ and a diffusivity $K_P = 1.7 \text{ K}^2 \text{ s}^{-1}$ is also introduced in the PV equation to insure numerical stability. As expected, the sensitivity to diffusivity is limited over the range of values tested; in particular, it does not affect the decay of the tracer maximum at first order. The value of K for the tracer was adjusted to reproduce the width of the front observed in the WRF simulation.

The heating $Q = \gamma \chi - \alpha(T - \bar{T})$ used in Eq. A21 and 13 is the one used in WRF (defined in Eq. 21) with $\gamma = 5 \text{ K/day}/(\text{kg/kg})$ and $\alpha = 2.2 \text{ day}^{-1}$. Contrary to the standard Burgers case, a complication here arises due the need to invert the temperature profile which can a priori only be inferred from knowledge of the radial structure; for simplicity, we use here a quasi-geostrophic ansatz to derive a direct formula relating the temperature anomaly to the perturbation of PV. This is, a priori, a crude approximation but has the advantage of simplicity. Under the quasi-geostrophic approximation (Berrisford et al., 1990), the full PV is approximated as

$$P = \frac{1}{\bar{\sigma}} (f + q)$$

where $\bar{\sigma} = -1/g(\partial p/\partial \theta)_{x,y}$ is a mean vertical profile which depends only on θ and q is the quasi-geostrophic potential vorticity which is defined as

$$f q = \nabla_{\theta}^2 M + \frac{f^2}{g \bar{\sigma}} \frac{\partial}{\partial \theta} \bar{\rho} \theta \frac{\partial M}{\partial \theta} \quad (\text{A22})$$

where $M = C_p T' + \phi'$ is the anomaly in the Montgomery potential with respect to the basic stratification. It satisfies

$$\left(\frac{\partial}{\partial t} + \mathbf{v}_g \cdot \nabla_{\theta} \right) q = \frac{f}{\bar{\sigma}} \frac{\partial(\bar{\sigma} \theta)}{\partial \theta} \quad (\text{A23})$$

with $\mathbf{v}_g = \left(-\frac{1}{f} \frac{\partial M}{\partial y}, \frac{1}{f} \frac{\partial M}{\partial x} \right)$ the geostrophic velocity.

Based on this, we derive the temperature from the anomaly P' of the PV along the axis for which $q = -\bar{\sigma} P'$. As no information on the radial dependency is available in this framework, we assume a scale factor ℓ such that $\nabla_{\theta}^2 M = -\ell^2 M$ in (A22). In the sake of simplicity, we also assume a uniform background temperature $\bar{T}(\theta) = T_1$ in the vertical domain of the vortex. The explicit formula for the perturbation temperature on the axis is then:

$$T'(\theta) = \frac{T_1}{2f} \left(- \left(1 + \frac{\kappa}{2\eta} \right) \int_{\theta}^{\infty} \left(\frac{\theta}{x} \right)^{\eta + \frac{1}{2\kappa}} q(x) \frac{dx}{x} + \left(1 - \frac{\kappa}{2\eta} \right) \int_{\theta_T}^{\theta} \left(\frac{x}{\theta} \right)^{\eta - \frac{1}{2\kappa}} q(x) \frac{dx}{x} \right) \quad (\text{A24})$$

where $\eta^2 = \frac{\ell^2 g^2}{f^2 N^2} + \frac{1}{4\kappa^2}$. Note that the temperature anomaly obtained from this QG inversion only takes the central PV profile into account and is not expected to reproduce exactly the actual evolution of the temperature field in the WRF simulation. The value of $1/\ell = 250 \text{ km}$ was adjusted to reproduce the depth of the temperature anomaly

at the initial time of the simulation. Nevertheless, the slight horizontal expansion of the vortex as it ascends is not represented in this constant ℓ and the agreement between WRF and 1D-model temperature anomaly deteriorates with time. To circumvent this issue and better reproduce the observed evolution of the tracer in the WRF simulation, α was increased by 50% compared to the value used in WRF.

Acknowledgements

This work was performed using HPC resources from GENCI-IDRIS (Grant 2022-AD010106852). This research has been supported by the Agence Nationale de la Recherche under grants 21-CE01-0007-01 (ASTuS) and 21-CE01-0016-01 (TuRTLES).

references

- Andrews, D., Holton, J., and Leovy, C.: Middle Atmosphere Dynamics., Academic Press, 1987.
- Aubert, O., Bars, M. L., Gal, P. L., and Marcus, P. S.: The Universal Aspect Ratio of Vortices in Rotating Stratified Flows: Experiments and Observations, *Journal of Fluid Mechanics*, 706, 34–45, URL <https://doi.org/10.1017/jfm.2012.176>, 2012.
- Baines, P. G. and Sparks, R. S. J.: Dynamics of Giant Volcanic Ash Clouds from Supervolcanic Eruptions, *Geophysical Research Letters*, 32, URL <https://doi.org/10.1029/2005GL024597>, 2005.
- Berrisford, P., Marshall, J. C., and White, A. A.: Quasigeostrophic Potential Vorticity Equation in Isentropic Coordinates, *J. Atmos. Sci.*, 50, 778–782, 1990.
- Boers, R., de Laat, A. T., Zweers, D. C. S., and Dirksen, R. J.: Lifting Potential of Solar-Heated Aerosol Layers, *Geophys. Res. Lett.*, 37, URL <https://doi.org/10.1029/2010GL045171>, 2010.
- Brewer, A. W.: Evidence for a World Circulation Provided by the Measurements of Helium and Water Vapour Distribution in the Stratosphere, *Quarterly Journal of the Royal Meteorological Society*, 75, 351–363, URL <https://doi.org/10.1002/qj.49707532603>, 1949.
- Bui, H., Yoden, S., and Nishimoto, E.: QBO-like oscillation in a three-dimensional minimal model framework of the stratosphere–troposphere coupled system, *SOLA*, 15, 62–67, 2019.
- Butchart, N.: The Brewer-Dobson Circulation, *Reviews of Geophysics*, 52, 157–184, URL <https://doi.org/10.1002/2013RG000448>, 2014.
- Cai, Z., Griessbach, S., and Hoffmann, L.: Improved Estimation of Volcanic SO₂ Injections from Satellite Retrievals and Lagrangian Transport Simulations: The 2019 Raikoke Eruption, *Atmospheric Chemistry and Physics*, 22, 6787–6809, URL <https://doi.org/10.5194/acp-22-6787-2022>, 2022.
- Carr, J. L., Horváth, Á., Wu, D. L., and Friberg, M. D.: Stereo Plume Height and Motion Retrievals for the Record-Setting Hunga Tonga-Hunga Ha'apai Eruption of 15 January 2022, *Geophysical Research Letters*, 49, e2022GL098131, URL <https://doi.org/10.1029/2022GL098131>, 2022.
- Chouza, F., Leblanc, T., Barnes, J., Brewer, M., Wang, P., and Koon, D.: Long-Term (1999–2019) Variability of Stratospheric Aerosol over Mauna Loa, Hawaii, as Seen by Two Co-Located Lidars and Satellite Measurements, *Atmospheric Chemistry and Physics*, 20, 6821–6839, URL <https://doi.org/10.5194/acp-20-6821-2020>, 2020.
- Cole, J. D.: On a quasi-linear parabolic equation occurring in aerodynamics, *Quarterly of Applied Mathematics*, 9, 225–236, URL <https://doi.org/10.1090/qam/42889>, 1951.

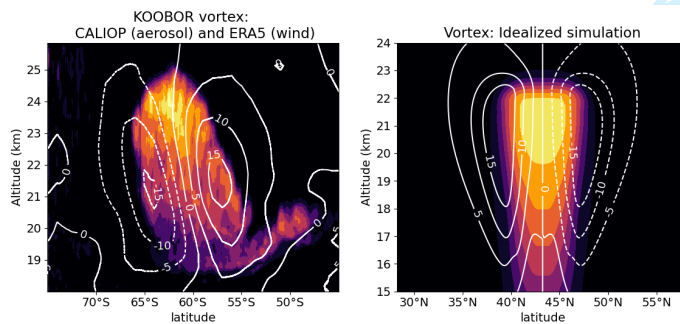
- de Laat, A. T. J., Stein Zweers, D. C., Boers, R., and Tuinder, O. N. E.: A Solar Escalator: Observational Evidence of the Self-Lifting of Smoke and Aerosols by Absorption of Solar Radiation in the February 2009 Australian Black Saturday Plume, *Journal of Geophysical Research: Atmospheres*, 117, URL <https://doi.org/10.1029/2011JD017016>, 2012.
- Doglioni, G., Aquila, V., Das, S., Colarco, P. R., and Zardi, D.: Dynamical Perturbation of the Stratosphere by a Pyrocumulonimbus Injection of Carbonaceous Aerosols, *Atmospheric Chemistry and Physics*, 22, 11 049–11 064, URL <https://doi.org/10.5194/acp-22-11049-2022>, 2022.
- Dritschel, D. G.: Vortex Merger in Rotating Stratified Flows, *Journal of Fluid Mechanics*, 455, 83–101, URL <https://doi.org/10.1017/S0022112001007364>, 2002.
- Eliassen, A.: Slow thermally or frictionally controlled meridional circulation in a circular Vortex, *Astrophys. Norv.*, 5, 60pp, 1952.
- Ertel, H.: Ein neuer hydrodynamischer Erhaltungssatz, *Die Naturwissenschaften*, 30, 543–544, URL <https://doi.org/10.1007/BF01475602>, 1942.
- Foussard, A., Lapeyre, G., and Plougonven, R.: Storm track response to oceanic eddies in idealized atmospheric simulations, *Journal of Climate*, 32, 445–463, 2019.
- Fromm, M., Lindsey, D. T., Servranckx, R., Yue, G., Trickl, T., Sica, R., Doucet, P., and Godin-Beekmann, S.: The Untold Story of Pyrocumulonimbus, *Bulletin of the American Meteorological Society*, 91, 1193–1210, URL <https://doi.org/10.1175/2010BAMS3004.1>, 2010.
- Garny, H. and Randel, W. J.: Dynamic Variability of the Asian Monsoon Anticyclone Observed in Potential Vorticity and Correlations with Tracer Distributions, *Journal of Geophysical Research: Atmospheres*, 118, 13,421–13,433, URL <https://doi.org/10.1002/2013JD020908>, 2013.
- Getzewich, B. J., Vaughan, M. A., Hunt, W. H., Avery, M. A., Powell, K. A., Tackett, J. L., Winker, D. M., Kar, J., Lee, K.-P., and Toth, T. D.: CALIPSO lidar calibration at 532nm: version 4 daytime algorithm, *Atmospheric Measurement Techniques*, 11, 6309–6326, URL <https://doi.org/10.5194/amt-11-6309-2018>, 2018.
- Gill, A. E.: Homogeneous Intrusions in a Rotating Stratified Fluid, *Journal of Fluid Mechanics*, 103, 275, URL <https://doi.org/10.1017/S0022112081001341>, 1981.
- Glaze, L. S., Baloga, S. M., and Wilson, L.: Transport of atmospheric water vapor by volcanic eruption columns, *Journal of Geophysical Research: Atmospheres*, 102, 6099–6108, URL <https://doi.org/10.1029/96JD03125>, 1997.
- Griffiths, R. W. and Linden, P. F.: The Stability of Vortices in a Rotating, Stratified Fluid, *Journal of Fluid Mechanics*, 105, 283–316, URL <https://doi.org/10.1017/S0022112081003212>, 1981.
- Hassanzadeh, P., Marcus, P. S., and Gal, P. L.: The Universal Aspect Ratio of Vortices in Rotating Stratified Flows: Theory and Simulation, *Journal of Fluid Mechanics*, 706, 46–57, URL <https://doi.org/10.1017/jfm.2012.180>, 2012.
- Haynes, P. H. and McIntyre, M. E.: On the Evolution of Vorticity and Potential Vorticity in the Presence of Diabatic Heating and Frictional or Other Forces, *Journal of the Atmospheric Sciences*, 44, 828–841, URL [https://doi.org/10.1175/1520-0469\(1987\)044<0828:OTEOVA>2.0.CO;2](https://doi.org/10.1175/1520-0469(1987)044<0828:OTEOVA>2.0.CO;2), 1987.
- Hersbach, H., Bell, B., Berrisford, P., Hirahara, S., Horányi, A., Muñoz-Sabater, J., Nicolas, J., Peubey, C., Radu, R., Schepers, D., Simmons, A., Soci, C., Abdalla, S., Abellan, X., Balsamo, G., Bechtold, P., Biavati, G., Bidlot, J., Bonavita, M., Chiara, G. D., Dahlgren, P., Dee, D., Diamantakis, M., Dragani, R., Flemming, J., Forbes, R., Fuentes, M., Geer, A., Haimberger, L., Healy, S., Hogan, R. J., Hólm, E., Janisková, M., Keeley, S., Laloyaux, P., Lopez, P., Lupu, C., Radnoti, G., Rosnay, P. d., Rozum, I., Vamborg, F., Villaume, S., and Thépaut, J.-N.: The ERA5 global reanalysis, *Quarterly Journal of the Royal Meteorological Society*, 146, 1999–2049, URL <https://doi.org/10.1002/qj.3803>, 2020.

- Holasek, R. E., Self, S., and Woods, A. W.: Satellite Observations and Interpretation of the 1991 Mount Pinatubo Eruption Plumes, *Journal of Geophysical Research: Solid Earth*, 101, 27 635–27 655, URL <https://doi.org/10.1029/96JB01179>, 1996.
- Hopf, E.: The partial differential equation $ut + uux = \mu xx$, *Communications on Pure and Applied Mathematics*, 3, 201–230, URL <https://doi.org/10.1002/cpa.3160030302>, 1950.
- Hoskins, B. J., McIntyre, M. E., and Robertson, A. W.: On the Use and Significance of Isentropic Potential Vorticity Maps, *Quarterly Journal of the Royal Meteorological Society*, 111, 877–946, URL <https://doi.org/10.1002/qj.49711147002>, 1985.
- Kablick, G. P., Allen, D. R., Fromm, M. D., and Nedoluha, G. E.: Australian PyroCb Smoke Generates Synoptic-Scale Stratospheric Anticyclones, *Geophysical Research Letters*, 47, URL <https://doi.org/10.1029/2020GL088101>, 2020.
- Kar, J., Vaughan, M. A., Lee, K.-P., Tackett, J. L., Avery, M. A., Garnier, A., Getzewich, B. J., Hunt, W. H., Josset, D., Liu, Z., Lucker, P. L., Magill, B., Omar, A. H., Pelon, J., Rogers, R. R., Toth, T. D., Trepte, C. R., Vernier, J.-P., Winker, D. M., and Young, S. A.: CALIPSO Lidar Calibration at 532 Nm: Version 4 Nighttime Algorithm, *Atmospheric Measurement Techniques*, 11, 1459–1479, URL <https://doi.org/10.5194/amt-11-1459-2018>, 2018.
- Khaykin, S., Legras, B., Bucci, S., Sellitto, P., Isaksen, I., Tencé, F., Bekki, S., Bourassa, A., Rieger, L., Zawada, D., Jumelet, J., and Godin-Beekmann, S.: The 2019/20 Australian Wildfires Generated a Persistent Smoke-Charged Vortex Rising up to 35 Km Altitude, *Communications Earth & Environment*, 1, 22, URL <https://doi.org/10.1038/s43247-020-00022-5>, 2020.
- Khaykin, S., Podglajen, A., Ploeger, F., Groß, J.-U., Tence, F., Bekki, S., Khlopenkov, K., Bedka, K., Rieger, L., Baron, A., Godin-Beekmann, S., Legras, B., Sellitto, P., Sakai, T., Barnes, J., Uchino, O., Morino, I., Nagai, T., Wing, R., Baumgarten, G., Gerding, M., Duflo, V., Payen, G., Jumelet, J., Querel, R., Liley, B., Bourassa, A., Clouser, B., Feoflov, A., Hauchecorne, A., and Ravetta, F.: Global Perturbation of Stratospheric Water and Aerosol Burden by Hunga Eruption, *Communications Earth & Environment*, 3, 1–15, URL <https://doi.org/10.1038/s43247-022-00652-x>, 2022a.
- Khaykin, S. M., Godin-Beekmann, S., Hauchecorne, A., Pelon, J., Ravetta, F., and Keckhut, P.: Stratospheric Smoke With Unprecedentedly High Backscatter Observed by Lidars Above Southern France, *Geophysical Research Letters*, 45, 1639–1646, URL <https://doi.org/10.1002/2017GL076763>, 2018.
- Khaykin, S. M., de Laat, A. T. J., Godin-Beekmann, S., Hauchecorne, A., and Ratynski, M.: Unexpected Self-Lofting and Dynamical Confinement of Volcanic Plumes: The Raikoke 2019 Case, *Scientific Reports*, 12, 22 409, URL <https://doi.org/10.1038/s41598-022-27021-0>, 2022b.
- Legras, B., Duchamp, C., Sellitto, P., Podglajen, A., Carboni, E., Siddans, R., Groß, J.-U., Khaykin, S., and Ploeger, F.: The Evolution and Dynamics of the Hunga Tonga–Hunga Ha’apai Sulfate Aerosol Plume in the Stratosphere, *Atmospheric Chemistry and Physics*, 22, 14 957–14 970, URL <https://doi.org/10.5194/acp-22-14957-2022>, 2022.
- Lestrelin, H., Legras, B., Podglajen, A., and Salihoglu, M.: Smoke-Charged Vortices in the Stratosphere Generated by Wildfires and Their Behaviour in Both Hemispheres: Comparing Australia 2020 to Canada 2017, *Atmospheric Chemistry and Physics*, 21, 7113–7134, URL <https://doi.org/10.5194/acp-21-7113-2021>, 2021.
- Long, R. R.: STEADY MOTION AROUND A SYMMETRICAL OBSTACLE MOVING ALONG THE AXIS OF A ROTATING LIQUID, *Journal of the Atmospheric Sciences*, 10, 197–203, URL [https://doi.org/10.1175/1520-0469\(1953\)010<0197:SMASD>2.0.CO;2](https://doi.org/10.1175/1520-0469(1953)010<0197:SMASD>2.0.CO;2), 1953.
- Meunier, P., Benjamin, M., and Dizès, S. L.: Instabilities around a Rotating Ellipsoid in a Stratified Rotating Flow, in: 19th Australasian Fluid Mechanics Conferences, 2014.
- Millán, L., Santee, M. L., Lambert, A., Livesey, N. J., Werner, F., Schwartz, M. J., Pumphrey, H. C., Manney, G. L., Wang, Y., Su, H., Wu, L., Read, W. G., and Froidevaux, L.: The Hunga Tonga–Hunga Ha’apai Hydration of the Stratosphere, *Geophysical Research Letters*, 49, e2022GL099381, URL <https://doi.org/10.1029/2022GL099381>, 2022.

- Ohneiser, K., Ansmann, A., Baars, H., Seifert, P., Barja, B., Jimenez, C., Radenz, M., Teisseire, A., Floutsi, A., Haarig, M., Foth, A., Chudnovsky, A., Engelmann, R., Zamorano, F., Bühl, J., and Wandinger, U.: Smoke of Extreme Australian Bushfires Observed in the Stratosphere over Punta Arenas, Chile, in January 2020: Optical Thickness, Lidar Ratios, and Depolarization Ratios at 355 and 532 nm, *Atmospheric Chemistry and Physics*, 20, 8003–8015, URL <https://doi.org/10.5194/acp-20-8003-2020>, 2020.
- Peterson, D. A., Fromm, M. D., McRae, R. H. D., Campbell, J. R., Hyer, E. J., Taha, G., Camacho, C. P., Kablick, G. P., Schmidt, C. C., and DeLand, M. T.: Australia's Black Summer Pyrocumulonimbus Super Outbreak Reveals Potential for Increasingly Extreme Stratospheric Smoke Events, *npj Clim Atmos Sci*, 4, 38, URL <https://doi.org/10.1038/s41612-021-00192-9>, 2021.
- Proud, S. R., Prata, A. T., and Schmauß, S.: The January 2022 Eruption of Hunga Tonga-Hunga Ha'apai Volcano Reached the Mesosphere, *Science*, 378, 554–557, URL <https://doi.org/10.1126/science.abo4076>, 2022.
- Pumphrey, H. C., Schwartz, M. J., Santee, M. L., Kablick III, G. P., Fromm, M. D., and Livesey, N. J.: Microwave Limb Sounder (MLS) Observations of Biomass Burning Products in the Stratosphere from Canadian Forest Fires in August 2017, *Atmospheric Chemistry and Physics*, 21, 16 645–16 659, URL <https://doi.org/10.5194/acp-21-16645-2021>, 2021.
- Reinaud, J. N. and Dritschel, D. G.: The Merger of Vertically Offset Quasi-Geostrophic Vortices, *Journal of Fluid Mechanics*, 469, 287–315, URL <https://doi.org/10.1017/S0022112002001854>, 2002.
- Schallock, J., Brühl, C., Bingen, C., Höpfner, M., Rieger, L., and Lelieveld, J.: Reconstructing volcanic radiative forcing since 1990, using a comprehensive emission inventory and spatially resolved sulfur injections from satellite data in a chemistry-climate model, *Atmospheric Chemistry and Physics*, 23, 1169–1207, <https://doi.org/10.5194/acp-23-1169-2023>, 2023.
- Schoeberl, M. R., Lait, L. R., Newman, P. A., and Rosenfield, J. E.: The structure of the polar vortex, *Journal of Geophysical Research*, 97, 7859, <https://doi.org/10.1029/91JD02168>, 1992.
- Schoeberl, M. R., Wang, Y., Ueyama, R., Taha, G., and Yu, W.: The Cross Equatorial Transport of the Hunga Tonga-Hunga Ha'apai Eruption Plume, *Geophysical Research Letters*, 50, e2022GL102443, URL <https://doi.org/10.1029/2022GL102443>, 2023.
- Schubert, W. H.: Bernhard Haurwitz Memorial Lecture (2017): Potential Vorticity Aspects of Tropical Dynamics, 2018.
- Schubert, W. H. and Alworth, B. T.: Evolution of Potential Vorticity in Tropical Cyclones, *Quarterly Journal of the Royal Meteorological Society*, 113, 147–162, URL <https://doi.org/10.1002/qj.49711347509>, 1987.
- Schubert, W. H. and Hack, J. J.: Transformed Eliassen Balanced Vortex Model, *Journal of the Atmospheric Sciences*, 40, 1571–1583, URL [https://doi.org/10.1175/1520-0469\(1983\)040<1571:TEBVM>2.0.CO;2](https://doi.org/10.1175/1520-0469(1983)040<1571:TEBVM>2.0.CO;2), 1983.
- Sellitto, P., Podglajen, A., Belhadji, R., Boichu, M., Carboni, E., Cuesta, J., Duchamp, C., Kloss, C., Siddans, R., Bègue, N., Blarel, L., Jegou, F., Khaykin, S., Renard, J.-B., and Legras, B.: The Unexpected Radiative Impact of the Hunga Tonga Eruption of 15th January 2022, *Communications Earth & Environment*, 3, 1–10, URL <https://doi.org/10.1038/s43247-022-00618-z>, 2022.
- Sellitto, P., Belhadji, R., Cuesta, J., Podglajen, A., and Legras, B.: Radiative impacts of the Australian bushfires 2019–2020 – Part 2: Large-scale and in-vortex radiative heating, *EGUsphere*, 2023, 1–19, <https://doi.org/10.5194/egusphere-2023-1067>, 2023.
- Senf, F., Heinold, B., Kubin, A., Müller, J., Schrödner, R., and Tegen, I.: How the extreme 2019–2020 Australian wildfires affected global circulation and adjustments, *EGUsphere*, 2023, 1–28, URL <https://doi.org/10.5194/egusphere-2023-113>, 2023.
- Shutts, G.: Some Exact Solutions to the Semi-Geostrophic Equations for Uniform Potential Vorticity Flows, *Geophysical & Astrophysical Fluid Dynamics*, 57, 99–114, URL <https://doi.org/10.1080/03091929108225230>, 1991.

- 1 Shutts, G. J. and Thorpe, A. J.: Some Aspects of Vortices in Rotating Stratified Fluids, *Pure and Applied Geophysics*, 116,
2 993–1006, URL <https://doi.org/10.1007/BF00874667>, 1978.
- 3
- 4 Shutts, G. J., Booth, M., and Norbury, J.: A Geometric Model of Balanced, Axisymmetric Flows with Embedded Penetrative
5 Convection, *Journal of the Atmospheric Sciences*, 45, 2609–2621, 1988.
- 6
- 7 Skamarock, C., Klemp, B., Dudhia, J., Gill, O., Barker, D., Duda, G., Huang, X.-y., Wang, W., and Powers, G.: A Description of
8 the Advanced Research WRF Version 3, URL <https://doi.org/10.5065/D68S4MVH>, 2008.
- 9
- 10 Smagorinski, J.: GENERAL CIRCULATION EXPERIMENTS WITH THE PRIMITIVE EQUATIONS: I. THE BASIC EXPERI-
11 MENT, *Monthly Weather Review*, 91, 99 – 164, [https://doi.org/https://doi.org/10.1175/1520-0493\(1963\)091<0099:GCEWTP>2.3.CO;2](https://doi.org/https://doi.org/10.1175/1520-0493(1963)091<0099:GCEWTP>2.3.CO;2), 1963.
- 12
- 13 Taylor, G. I.: The Motion of a Sphere in a Rotating Liquid, *Proceedings of the Royal Society of London. Series A, Containing
14 Papers of a Mathematical and Physical Character*, 102, 180–189, URL <https://doi.org/10.1098/rspa.1922.0079>, 1922.
- 15
- 16 Thorpe, A. J.: Diagnosis of Balanced Vortex Structure Using Potential Vorticity, *Journal of the Atmospheric Sciences*, 42,
17 397–406, URL [https://doi.org/10.1175/1520-0469\(1985\)042<0397:DOBVSU>2.0.CO;2](https://doi.org/10.1175/1520-0469(1985)042<0397:DOBVSU>2.0.CO;2), 1985.
- 18
- 19 Vanneste, J. and Haynes, P. H.: Intermittent Mixing in Strongly Stratified Fluids as a Random Walk, *Journal of Fluid Mechanics*,
20 411, 165–185, URL <https://doi.org/10.1017/S0022112099008149>, 2000.
- 21
- 22 Vaughan, M. A., Young, S. A., Winker, D. M., Powell, K. A., Omar, A. H., Liu, Z., Hu, Y., and Hostetler, C. A.: Fully automated
23 analysis of space-based lidar data: an overview of the CALIPSO retrieval algorithms and data products, *Proc. SPIE 5575,*
24 *Laser Radar Techniques for Atmospheric Sensing*, (4 November 2004), URL <https://doi.org/10.1117/12.572024>, 2004.
- 25
- 26 Whitham, G. B.: Burgers' Equation, chap. 4, pp. 96–112, John Wiley & Sons, Ltd, <https://doi.org/https://doi.org/10.1002/9781118032954.ch4>, 1999.
- 27
- 28 Winker, D. M., Pelon, J., Jr, J. A. C., Ackerman, S. A., Charlson, R. J., Colarco, P. R., Flamant, P., Fu, Q., Hoff, R. M., Kittaka, C.,
29 Kubar, T. L., Treut, H. L., McCormick, M. P., Mégie, G., Poole, L., Powell, K., Treppe, C., Vaughan, M. A., and Wielicki, B. A.:
30 The CALIPSO mission: A Global 3D View of Aerosols and Clouds, *Bulletin of the American Meteorological Society*, 91,
31 1211–1230, 2010.
- 32
- 33 Yu, P., Toon, O. B., Bardeen, C. G., Zhu, Y., Rosenlof, K. H., Portmann, R. W., Thornberry, T. D., Gao, R.-S., Davis, S. M., Wolf, E. T.,
34 de Gouw, J., Peterson, D. A., Fromm, M. D., and Robock, A.: Black carbon lofted wildfire smoke high into the stratosphere
35 to form a persistent plume, *Science*, 365, 587–590, URL <https://doi.org/10.1126/science.aax1748>, 2019.

36 GRAPHICAL ABSTRACT



45 Satellite and reanalysis data
46 have revealed the organi-
47 zation of stratospheric plumes
48 from extreme wildfires and
49 volcanic eruptions into synoptic-
50 scale anticyclones. Previ-
51 ous research recognized
52 the role of radiative heat-
53 ing from sunlight-absorbing
54 aerosols in this phenomenon.

55 Here, a reduced model is introduced which attributes the structures to diabatic forcing by a Lagrangian tracer. By in-
56 vestigating the forced flow using potential vorticity theory and comparing analytical results to numerical simulations,
57 the study offers the first comprehensive understanding of this atmospheric occurrence.